Self-correction of the optical distortion effect of thermal plumes in particle image velocimetry

Xiyuan Bao^{1,} a) and Carolina Lithgow-Bertelloni¹ Department of Earth, Planetary, and Space Sciences, University of California

(Dated: 4 May 2025)

Optical distortion caused by changes in the refractive index of fluid flow is a common issue in flow visualization using techniques such as Particle Image Velocimetry (PIV). In thermally-driven convection, this distortion can severely interfere with PIV results due to the ubiquitous density and therefore refractive index heterogeneity in the fluid. The distortion also varies spatially and temporally, adding to the challenge. We propose a composite filter, the SA-PIVR filter, which combines a series of conventional image filters to address this issue, focusing on optical distortion of thermal plumes in laminar flow. For the first time, we effectively mitigate the optical distortion from plumes while preserving the in-plane plume velocity and overall flow pattern, with the PIV data alone. Our filter is efficient and does not require additional measurements, expensive ray tracing, or a large dataset to begin with. It can be extended to separate the flow field and the effect of optical distortion in other fluid experiments when the two components are visually distinct. Additionally, this filter can serve as a baseline algorithm for comparison when developing more advanced methods like neural networks.

I. INTRODUCTION

3

6

10

11

12

13

14

15

16

17

18

19

20

21

22

23

25

26

27

31

32

34

37

38

40

42

43

Particle Image Velocimetry (PIV) is a widely utilized tech-52 nique for measuring flow velocity. The fundamental prin-53 ciple of PIV involves tracking clusters of seeding particles 54 or tracers between two sequentially captured frames of the 55 same illuminated plane, using cross-correlation to determine 56 their displacement 11. This displacement is typically attributed 57 solely to fluid flow. However, when fluid density heterogene-58 ity is present, it leads to changes in the refractive index and 59 perturbations in the light ray paths from the tracers to the 60 camera². Such density heterogeneity can result from volume 61 changes in compressible fluids due to external forces (e.g., 62 shock waves in air or thermally-driven convection. In the 63 presence of refractive index anomalies in the fluid, the posi-64 tion, shape, and displacement of tracers result from both the 65 flow and the fluid density distribution, which can pose sig-66 nificant challenges in interpreting PIV results². This is es-67 pecially severe for PIV imaging of thermal convection ex-68 periments in viscous fluids where the flow is dominated by 69 plumes/thermals 156. The ubiquitous plumes change the light 70 ray path within the whole fluid domain, cast shadows in planes 71 behind the plumes, and corrupt the PIV results. From here on 72 out, we refer to these optical distortions on the particle image 73 as "plume shadow" and the affected region of PIV vectors as 74 Shadow-Affected PIV Region (SA-PIVR) for short.

Previous studies have tried to account for optical distor- ⁷⁶ tion effects in PIV by mapping the distorted particle images ⁷⁷ to the undistorted state, or by directly correcting the affected ⁷⁸ PIV vectors ²¹⁷¹ The proposed solutions were limited to ⁷⁹ simplified scenarios (e.g., 2D steady flow or fixed distor- ⁸⁰ tions), depended on additional distortion measurements (cf. ⁸¹ Sec. III), and usually relied on computationally expensive ray tracing ¹¹⁰¹ For time-dependent flow, where all particle

images are distorted differently, these solutions are not adequate, and the additional measurements and computational cost make them impractical or prohibitive.

Here, we build a filter based on the combination of a series of conventional image filters, to correct the SA-PIVR. The filter removes visually distinct regions of corrupted PIV results. Our method is efficient and robust and does not require additional measurements, or large synthetic datasets, which are hard to produce for time-dependent flow, or with computationally expensive ray tracing. It needs only the existing PIV data. Because of its efficiency, our filter is suitable for processing the massive datasets produced by scanning PIV for long experiments. Though we focus on viscous thermal convection, the filter can be effective as long as the length scale of the shadow affected PIV region is smaller than that of the in-plane flow. We also show that the distortions are more than a nuisance and they provide quantitative clues on plume morphology.

We first review previous solutions to the PIV optical distortion in the literature (Sec. [II]), followed by a theoretical derivation of the origin of the optical distortions coupled with an analysis of the plume shadow and corresponding SA-PIVR in a thermal convection experiment Sec. [III]). In Sec. [IV] we introduce the workflow and the design of the PIV plume filter to remove SA-PIVR. We validate our method with a synthetic test, and present quality assessment, error analysis, and energy spectra compared to the PIV results on undistorted images in Sec. [V] In the last two sections, we apply the filters to a laboratory experiments of Rayleigh-Bénard convection in a very viscous fluid (Sec. [VI]) and discuss other implications of the plume shadow and broader applications of the filter. We conclude with a final summary in Sec. [VII]

II. PREVIOUS SOLUTIONS TO THE PIV OPTICAL DISTORTION

Extensive previous efforts have been directed towards PIV optical distortion due to a refractive index *n* anomaly fixed in

space and time (e.g., the wall of the test section or air outside144 the test section). The distorted particle images are "dewarped"145 to the undistorted state, using a back-projection function that 146 matches the experimentally obtained image with a calibra-147 tion target Alternatively, ray tracing through the known₁₄₈ refractive index field n can be performed to dewarp the parti-149 cle images or correct the PIV vectors directly. A hybrid₁₅₀ method combining the approaches described above has been₁₅₁ developed and applied to PIV experiments with a known mov-152 ing *n* anomaly by Zha *et al.* However, the fluid's refractive₁₅₃ index or density distribution is usually not directly available. 154

87

88

91

93

97

98

100

101

103

105

106

108

109

110

111

112

113

115

116

118

119

121

122

124

126

127

128

130

131

133

134

136

137

139

140

142

Elsinga *et al.* pointed out that Background Oriented ¹⁵⁵ Schlieren (BOS) a can be a useful tool to estimate n of the ¹⁵⁶ fluid itself and to evaluate the PIV error introduced by optical157 distortion. BOS relies on a high contrast pattern (e.g., random¹⁵⁸ dots) at the back of the fluid of interest (usually air). In BOS,159 the camera will capture the image without any optical distor-160 tion as the reference, and an image through the working fluid¹⁶¹ which shows the distortion. By comparing the two images using cross-correlation, one can obtain the displacement of the background dots integrated through the n anomalies. Note that 162 here BOS and PIV are both affected by optical distortion, but the background pattern in BOS is static, while the illuminated163 particles in PIV are dynamic.

Elsinga et al. suggested that the PIV error due to optical 164 distortion can be decomposed into the PIV vector position¹⁶⁵ error and the velocity error. They were able to analyze and correct the PIV results based on BOS but with several assumptions and simplifications not applicable to 3D transient 166 flow (e.g. thermal convection): steady 2D flow and n field, 167 and air as the working and ambient fluid. In 3D flow, the₁₆₈ 3D refractive index field needs to be reconstructed using ray₁₆₉ tracing for every single frame, which typically requires more cameras and corresponding BOS backgrounds 1516. Such a configuration and the required inverse reconstruction problem₁₇₀ are hard and computationally expensive. Adding a simultaneous PIV system to acquire the BOS images would signifi-171 cantly increase the cost and computational challenge (Elsinga et al. only performed single-camera asynchronous PIV/BOS₁₇₂ measurements). Even with all the additional data, the PIV_{173} algorithm may still fail to find the correct tracer pair in the₁₇₄ presence of large optical distortions!

More recently deep learning algorithms have been used for 175 general planar-PIV tasks. They are usually end-to-end methods that directly convert particle image pairs to final velocities₁₇₆ using trained neural networks. Training the neural networks requires large datasets (1000 to 10000) of particle image pairs₁₇₇ with corresponding ground truth velocities 17118. Very few 178 studies have applied deep learning to PIV with optical distortions. Gao et al. [13] provided a special example in which the water-air interface caused optical distortions in planar PIV. Their experimental setup allowed them to use a deformable mirror to simulate the water-air interface and obtain both the distorted and undistorted PIV images in situ. A wavefront sen-180 sor simultaneously measured the interface topography. With these measurements they obtained 20,000 pairs of PIV im-181 ages and water-air interface data to train a Convolutional Neu-182 ral Network (CNN) which dewarped the optically distorted₁₈₃

PIV image to its undistorted state. Unfortunately, their success with a semi-2D refractive index anomaly (water-air interface) does not apply to 3D flow and n anomaly within the fluid domain: The undistorted particle images would not be accessible experimentally, because the tracer distribution changes with the time-dependent flow. In addition, creating a sufficiently large synthetic dataset of particle images, requires computationally expensive ray tracing and direct numerical simulations of the fluid flow, with no guarantee they would be faithful one-to-one replicas of the experimental flow.

To our knowledge, there are no existing practical solutions to remove the PIV optical distortion from 3D transient flow. We have developed one based on the PIV data and the visually distinct SA-PIVR. It takes advantage of the difference between the distorted and undistorted regions in the raw particle images or PIV vectors. It allows for self-correction of the distortion without additional measurements or computationally expensive numerical simulations/ray tracing.

PLUME SHADOW AND SA-PIVR

Optical displacement generated by plumes

When a light ray passes through a medium with a density and refractive index gradient, it follows Snell's law²⁰:

$$n\sin\theta = C. \tag{1}$$

where θ is the incident angle and C is a constant. The differential form of Eq. I can be obtained by taking the derivative on both sides:

$$-\cot\theta \,d\theta = \frac{dn}{n}$$

$$\tan\phi \,d\phi = \frac{dn}{n}.$$
(2)

$$\tan \phi \, \mathrm{d}\phi = \frac{\mathrm{d}n}{n}.\tag{3}$$

with ϕ as the complementary angle of θ . If we limit the light ray to the x - y plane and let n = n(y), $\tan \phi = dy/dx$. Eq. 3 is then transformed into

$$\mathrm{d}\phi = \frac{1}{n} \frac{\mathrm{d}n}{\mathrm{d}y} \mathrm{d}x \tag{4}$$

$$\Delta \phi = \int \frac{1}{n} \frac{\mathrm{d}n}{\mathrm{d}y} \mathrm{d}x. \tag{5}$$

Eq. 5 provides the deflection angle after traveling through the density gradient. In 3D a general form can be written as:

$$\Delta \phi = \int \frac{1}{n} \nabla n \mathrm{d}x. \tag{6}$$

$$\xi_a = (Z_D + Z_d) \tan \Delta \phi \approx Z_D \Delta \phi \approx \frac{Z_D}{n_0} \int \nabla n dz.$$
 (7)

When the ambient medium and the working fluid are the same (e.g., PIV in air, Fig. 1), the displacement ξ seen by the camera is given by:

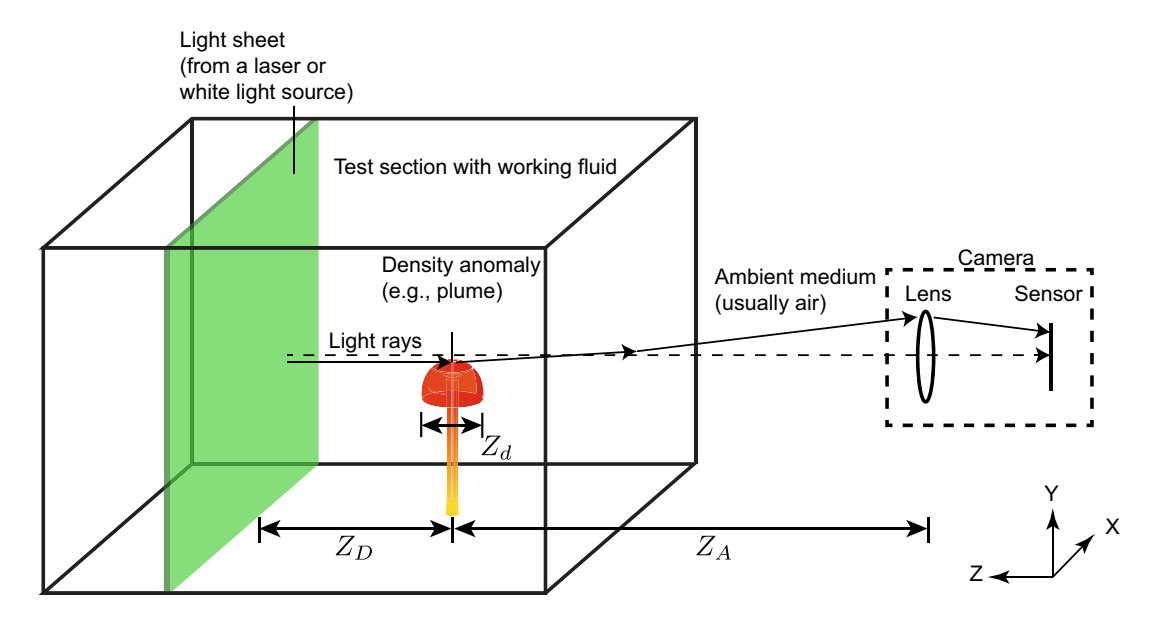


FIG. 1. Schematic cartoon of the light ray path responsible for the plume shadow considered in this study.

$$\xi = M\xi_a = M\frac{Z_D}{n_0} \int \nabla n dz. \tag{8}$$

where the magnification factor $M = \frac{f}{Z_D + Z_A - f}$, here Z_A is the²¹³ distance from the density gradient to the lens (Fig. []), and²¹⁴ f is the focal length of the lens. For liquids including air,²¹⁵ water, and syrup, the refractive index can be described with²¹⁶ the Gladstone-Dale relation:

$$n = 1 + K\rho. \tag{9}$$

$$\nabla n = K \nabla \rho. \tag{10}^{221}$$

where ρ is the fluid density, and K is the fluid-dependent₂₂₃ Gladstone-Dale constant. Eq. 8 now becomes:

$$\xi = M\xi_a = M\frac{Z_D}{n_0} \int K\nabla \rho dz.$$
 (11)₂₂₇

This ξ expression not only applies to PIV affected by opti-²²⁹ cal distortion but also to BOS²¹¹ and shadowgraphs¹²². As ρ is solution in the fluid temperature T, thermal anoma-²³¹ lies are n anomalies. We discuss n instead of ρ for the rest of the paper.

From Eq. [8] the optical displacement is proportional to the²³⁴ integrated ∇n along the ray path. In viscous thermal convec-²³⁵ tion experiments dominated by plumes, ∇n is the largest near²³⁶ the edge of the plumes as seen in shadowgraphs [23].

An estimate of the optical displacement ξ can be calculated₂₃₈ from Eq. 8. However, complexities arise when the ambient₂₃₉ medium (e.g., air) is not the same as the working fluid (e.g.,₂₄₀ syrup), as we discuss in Sec. V Instead, the optical displace-₂₄₁ ment can be directly measured from particle images such as₂₄₂ those in Fig. 2a,b, as we show below.

B. Effects of optical distortions induced by in-plane and out-of-plane flow on PIV vectors

Figure 2a,b illustrate these distortive optical effects in the raw particle images acquired during an experiment of vigorous thermal convection experiments in a viscous fluid heated from below (c.f. Sec. \overline{VIA}). The flow is dominated by thermal plumes with large (up to $\sim 5\%$) variation in refractive index. Around the plume head and stem the tracers are often elongated. Parallel linear segments perpendicular to the edges of the plume head are particularly obvious (Fig. 2b). Away from the edge of a plume head, including in its interior, the optical distortions are more subtle.

PIV algorithms match similar patches in particle image pairs. However, plume shadows complicate this process. Time-dependent fluid flow not only alters in-plane tracer configurations but also causes varying optical distortions between frames. The PIV algorithm attempts to match these distorted patches, which may include different optical displacements and elongation of already different tracers (displacement into or outside the illuminated plane). This complexity contrasts with the 2D steady flow case studied by Elsinga *et al.*²², where the optical distortion is fixed in time. Hence, the resulting SA-PIVR is a product of a nonlinear process in the time-dependent flow. This nonlinearity stems from frame-to-frame differences in optical distortion and tracer patterns, despite the optical displacement being proportional to the integrated refractive index anomalies (Eq. 8).

To quantify how the PIV results are affected by the shadows cast by plumes in front of the illuminated planes of interest, we first compute the lateral displacement from multiple methods. Fig. 2 c, d show the lateral displacement captured by optical flow and cross-correlation based PIV (CCPIV) combined with the Window Deformation Iterative Multi-grid scheme (WiDIM) 2526 . We use a 32×32 pixels CCPIV win-

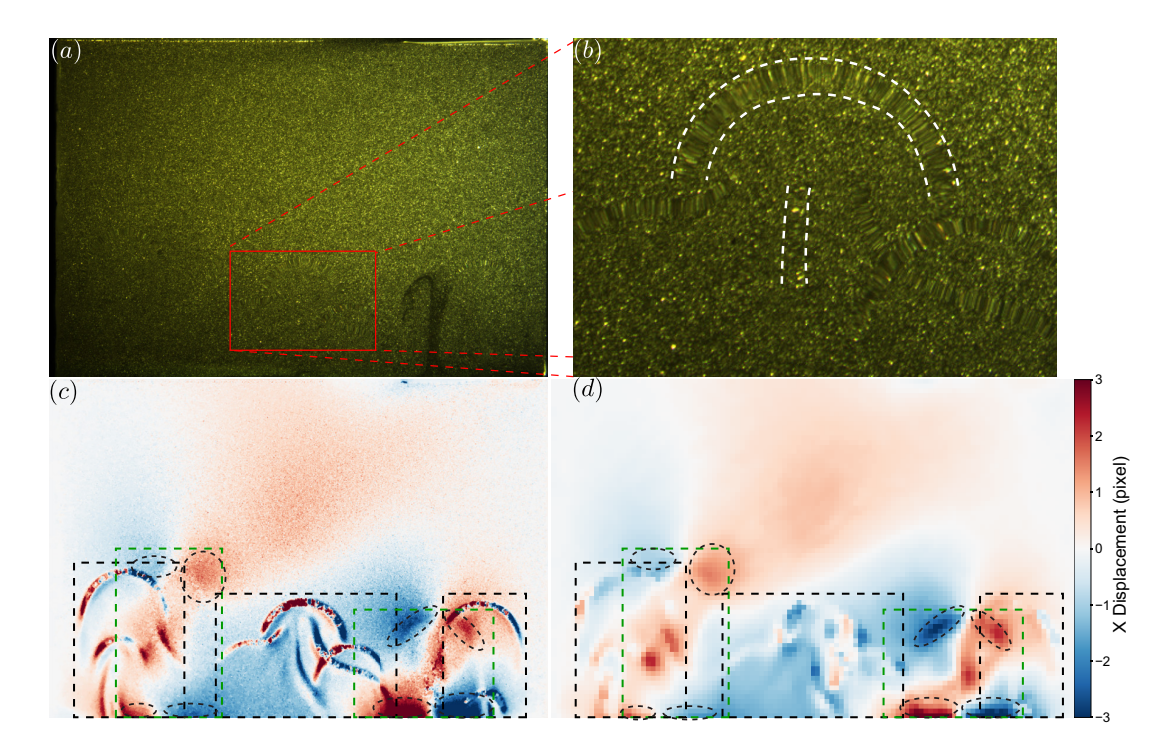


FIG. 2. Example of Particle Image Velocimetry with optical distortion from the experiment in Sec. VIA (a) Raw Image from a thermal convection experiment. Red rectangle outlines the zoomed panel in (b), where dashed white lines outline the tracer elongation from the distortions caused by the shadows of plumes in front of the illuminated plane. (c) Lateral displacement from optical flow (d) Lateral displacement from cross correlation and WiDIM Dashed green boxes bound the in-plane plumes. Dashed black boxes bound the SA-PIVR caused by the shadows cast by plumes in front of the illuminated plane. Dashed ovals bound the plume core, the fastest part of each in-plane plume. SA-PIVR appear as discontinuous bands.

dow with 50% overlapping. We further apply a standard $3 \times 3_{271}$ median filter $\overline{^{127}}$ to the CCPIV results. Optical flow provides a_{272} denser (per-pixel) velocity estimation compared to the lower a_{273} resolution CCPIV. The black dashed line boxes in Fig. $\overline{^{12}}$ c, a_{274} d bound the SA-PIVR. It is thin and sharp, while that from a_{275} the in-plane plume flow, bounded by dashed line green boxes, a_{276} is broad and smooth. This is particularly clear in the optical a_{277} flow results (Fig. a_{275}) and we will focus on optical flow results when analyzing SA-PIVR. Although the optical distortion in the particle image may be subtle, the corresponding SA-PIVR is distinct.

244

245

247

248

250

251

253

254

255

257

258

259

260

261

263

264

266

267

269

270

To better understand the SA-PIVR, its characteristics thick-282 ness, and differences with the PIV of in-plane plume flow,283 we look carefully at the distortions caused by the head of a284 plume in front (between the plane and the camera) of the illu-285 minated plane (p_{if}) . It is a region away from in-plane plumes₂₈₆ (p_{ip}) where the in-plane flow is near zero, so the direction₂₈₇ and amplitude of the PIV vectors are dominated by the optical₂₈₈ distortion alone (Fig. 3a,b). This part of the plume shadow₂₈₉ consists of two layers: the outer layer with parallel line seg-290 ments perpendicular to the plume head, and the inner layer₂₉₁ that still shows the dot pattern in tracers. The two layers have₂₉₂ a comparable thickness (about 6 mm), which is also the up-293 per bound of the optical displacement based on the extent of₂₉₄ the tracer elongation (Fig. 3a). For the outer layer, tracers at₂₉₅ the inner edge experience strong outward elongation, and vice₂₉₆ versa. In the inner layer, the optical distortion is subtle. A₂₉₇

close comparison of the two image frames reveals weak outward stretching. We interpret the outer layer to result from light rays traveling near the top edge of p_{if} , where $|\nabla T|$ and $|\nabla n|$ are the strongest [28] (Fig. 1). The inner layer should instead receive light rays that pass through the interior and lower part of the head of p_{if} , which has a much smaller $|\nabla T|$ and $|\nabla n|$.

As the p_{if} grows, the head becomes larger and sits higher in frame 1 (t_1) compared with frame 0 (t_0) . The outer layer correspondingly migrates upwards. Consequently, the tracers originally atop the outer layer in frame 0 are now elongated inward in frame 1: tracers located at the inner edge of the outer layer, originally elongated outward, are now destretched. The changes in the two layers are easily detected by optical flow (Fig. 3c). The inner shadow layer simply presents an outward flow, consistent with weak stretching. The outer shadow layer shows inward displacement overall, dominated by inward elongation of tracers atop the outer layer in frame 0 (Fig. 3a). Locally, the PIV algorithm is also affected by the outward elongation of tracers near the inner edge of the outer layer (dashed box in Fig. 3c). The thickness of the SA-PIVR shown here is the largest amongst all areas affected by optical distortions from the out of plane plumes (\sim 6 mm, Fig. 2c, Fig. 3c), but still less than half of the typical thickness of the head from in-plane plumes (Fig. 3d). The ambient in-plane flow is even broader. The SA-PIVR computed with optical flow is visually distinct (usually with large apparent displacement amplitude

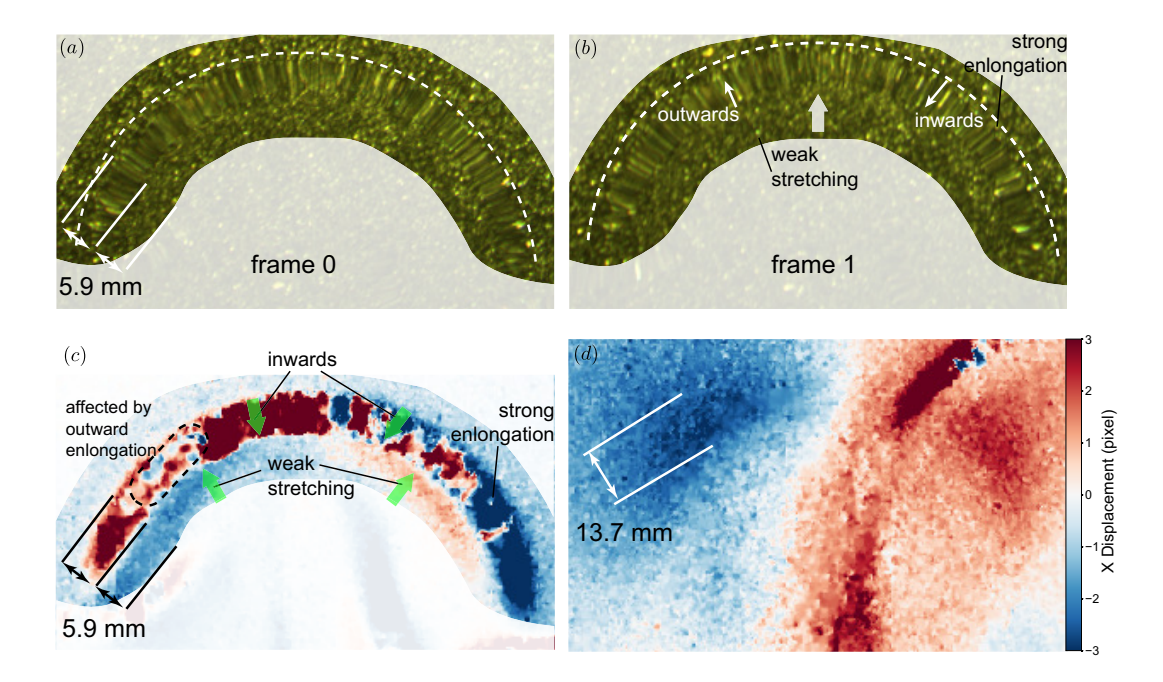


FIG. 3. Raw particle images of distortion in the plume head and corresponding SA-PIVR of the illuminated plane. (a) Raw particle images of the head of the plume shadow frame 0. (b) Like (a) but for frame 1. The plume shadow includes an outer layer with strong tracer elongation (outwards for tracers near the inner edge and vice versa (thin white arrows), and an inner layer undergoing weak outward stretching (thick white arrow). (c) Corresponding X displacement from optical flow. The inner layer shows outward movement, but the outer layer shows overall inward movement. The thicknesses of the two layers are comparable (double-sided arrows in (c) and (a)), but much smaller than the typical thickness of the in-plane plume flow (double-sided arrow in (d)). (d) Zoomed-in view of the right green box in Fig. [2].

of ~ 3 pixels) compared with the in-plane flow for the same₃₁₈ image pair. Thanks to these two characteristics, the SA-PIVR can be separated from the largest displacements (dashed line₃₁₉ ovals in Fig. [2c,d) caused by the fastest part of each in-plane₃₂₀ plume ("plume core"). In lateral displacement as shown here,₃₂₁ near the roots and heads (Fig. [2c), and vertically along the₃₂₂ plume stem.

The results are similar using a CCPIV algorithm (Fig. 2d). $_{324}$ Although CCPIV can only produce lower resolution results $_{325}$ compared to optical flow, we again find the characteristic $_{326}$ length scale of the plume core to be typically twice as thick $_{327}$ as that of the SA-PIVR (Fig. 2c). If no distinguishable, dis- $_{328}$ tinct, SA-PIVR exists, it is safe to assume that ∇n and the $_{329}$ accompanying optical distortion along the ray path are negligible.

IV. THE PIV PLUME FILTER

Based on the analysis above we construct a workflow for a_{339} filter to be applied to the SA-PIVR. We refer to this filter as the PIV plume filter. The proposed workflow is shown in Fig.₃₄₀

A. Workflow

- 1. Run CCPIV algorithm on the particle image pair of interest and use a 3 × 3 median filter, which helps further reduce the thickness of the SA-PIVR ("Raw CCPIV", Fig. 4a).
- Perform non-local means filter on the Raw CCPIV result using a large search window size S_Ω, template window size S_ℬ, and filter strength h (e.g., 21 × 21, 7 × 7, 20, respectively, Fig. 4b). Calculate the absolute difference before and after (Fig. 4c). Additional median filters can be used in preprocessing to enhance the differences.
- 3. Use a threshold to convert the highlighted region in step 2 to a binary mask (Fig. 4d).
- 4. Perform morphological opening on the previous mask to remove the SA-PIVR and obtain a final mask, containing mostly the plume core region (Fig. 42).
- 5. Combine the raw CCPIV result within the plume core mask (Fig. 4f), and the non-local means result outside the plume core mask (Fig. 4g) and stitch them together (Fig. 4h). The displacement can be scaled up (×1.1) to compensate for the loss of amplitude in the next step.
- 6. Perform non-local means again on the stitched result, with small S_{Ω} , $S_{\mathcal{B}}$, h (e.g., 9×9 , 3×3 , 3, respectively,

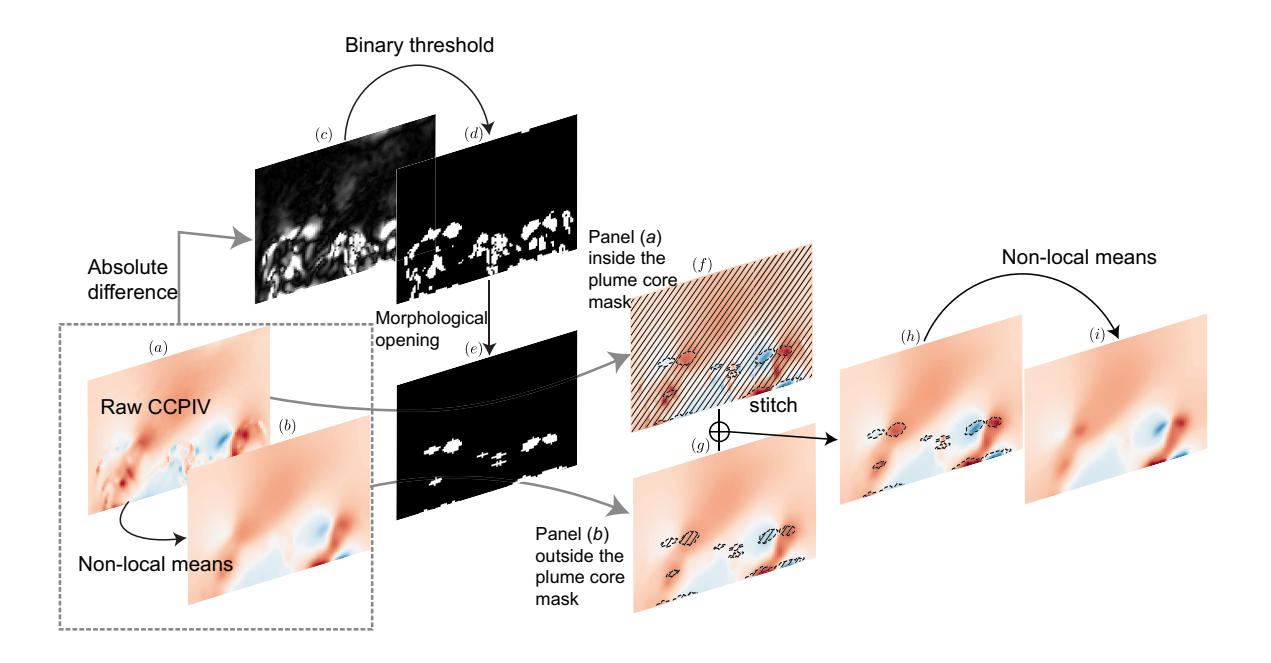


FIG. 4. Flowchart for the PIV plume filter.

374

375

376

Fig. 4b). This step can smooth out the stitching bound-368 ary from step 5, and any remaining SA-PIVR.

the original image *I* by:

This workflow largely removes the SA-PIVR, fills it with interpolated PIV data from its neighborhood, and preserves the overall in-plane flow pattern and the strength of the inplane plume flow (defined as the amplitude of the displacement in the plume core). Key to the filter's success is the construction of masks (steps 2, 4, and 6) for the SA-PIVR and separately for the in-plane plume flow. Below, we offer further details of the masks obtained by combining non-local means and morphological opening image filters.

B. Non-local means filter

342

343

345

346

347

348

349

351

352

354

355

356

357

358

359

360

362

363

366

367

Both the plume core and the SA-PIVR are characterized by $_{378}$ large displacements in the PIV image, and/or high displace- $_{379}$ ment gradients. Common gradient filters only sensitive to $_{380}$ high gradients are therefore inadequate at highlighting the af- $_{381}$ fected region. These include the Sobel X (Fig. 5b) and Sobel $_{382}$ Y filters, (Fig. 5c) which are based on the gradient of lateral $_{383}$ displacement along the x or y directions, and the Laplacian $_{384}$ (Fig. 5d) of the displacement. The non-local means filter we use in step 2 is a more effective "gradient detector", which $_{386}$ offers a finite filtering window size instead of only focusing $_{387}$ on every two pixels.

The non-local means filter is an image denoising algo- 389 rithm that averages pixels of similar neighborhoods. A fil- 390 tered single-channel (gray) image I_{NL} can be obtained from 391

$$I_{NL}(i) = \frac{1}{C(i)} \sum_{j \in \Omega(i)} w(i, j) I(j)$$
 (12)

$$w(i,j) = \exp\left(-\frac{|I(\mathcal{B}(i)) - I(\mathcal{B}(j))|^2}{h^2}\right). \tag{13}$$

where i and j are the pixel index (or vector index for CCPIV), C(i) is a normalization factor, $\Omega(i)$ is a search window centered at i with a size S_{Ω} , w(i, j) is the weighting factor, $\mathcal{B}(i)$ is the template window centered at i with a size $S_{\mathcal{B}}$, h is the filter strength. The proper setup of w(i, j) enables the non-local means filter to only average similar patches (template window) within a larger search window with a strength controlled by h. With a large search window size (e.g., $S_{\Omega} = 21 \times 21$) and template window size (e.g., $S_{\mathcal{B}} = 7 \times 7$), and a large filter strength (h = 20), we can smooth out small-scale features but still preserve the large-scale differences. Conversely, small search and template windows and small h apply a more modest smoothing but retain more texture locally. By taking the absolute difference of the CCPIV results before and after applying the non-local means mask (Fig. 2d), we effectively highlight the plume core and the SA-PIVR. The latter have sharp boundaries (green and red dashed line boxes in Fig. 5a). A pixel can be replaced by the location of each PIV vector when applying the non-local means filter to the PIV results. We now have an image with sharp boundaries, which allows us to create a binary mask using just a threshold value.

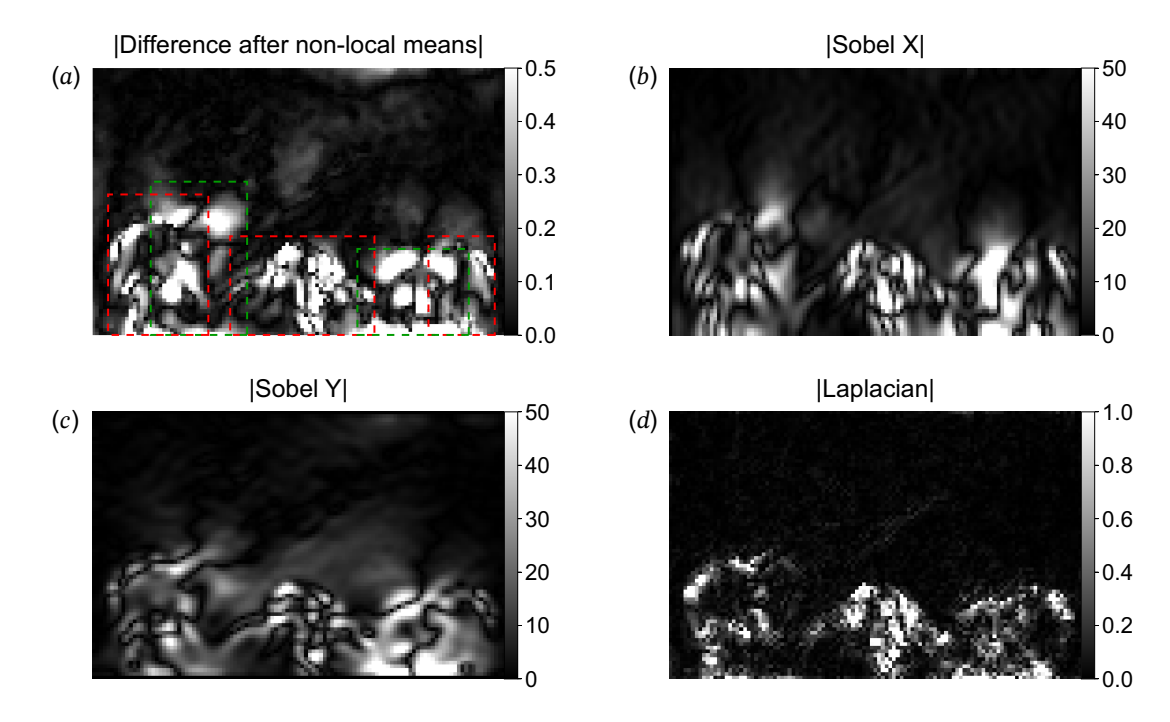


FIG. 5. Comparison of the gradients detected in lateral displacement in the SA-PIVR in Fig. 21. (a) Absolute difference before and after the non-local means filter (after additional median filters). The SA-PIVR and the in-plane plume are bounded by red and green dashed line boxes, respectively. (b) Amplitudes using Sobel X. (c) Sobel Y. (d)Laplacian filters.

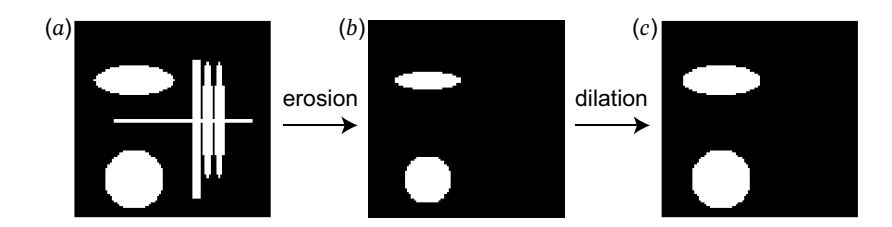


FIG. 6. The steps of morphological opening. (a) A binary mask with wide and thin features. (b) Erosion operation on (a). (c) Dilation operation on (b)

C. Morphological opening

393

394

396

397

399

400

401

402

403

405

406

To separate the plume core from the distinct, thinner and $_{411}^{11}$ discontinuous SA-PIVR bands (c.f. Fig. 2d), we adopt an $_{412}^{12}$ image processing tool called morphological opening $_{30}^{30}$. Mor- $_{413}^{12}$ phological opening is comprised of two steps: erosion and dilation (Fig. 6). A structuring element B (e.g., a square, an ellipse) is used to sweep the image A that contains our binary mask. For a patch of A that the structuring element completely fits within, the erosion step will remove boundary pixels, and the subsequent dilation step will restore the size of the remain- 415 ing shapes. Choosing B with a size between the wider and thinner features, we can effectively remove the thinner fea- 416 tures (Fig. 6b), while keeping the wider ones with their orig- 417 inal size. Ideally, morphological opening helps to produce 418 mask with only the core region of the plume.

V. TESTING THE FILTER WITH SYNTHETIC IMAGES

To verify the validity of the proposed PIV plume filter, we introduce a synthetic test based on ray tracing. We also provide qualitative and quantitative evaluation of the filter against the synthetic particle images generated from a numerical simulation of vigorous thermal convection in a viscous fluid and dominated by plumes.

A. Setup of the synthetic test

1. Overall configuration

We follow Fig. \blacksquare to design the synthetic test. We created particle images very similar to the experiment (c.f. Sec. $\boxed{\text{VI}}$) (Fig. $\boxed{2}$). The nominal test section is 40 cm \times 40 cm \times 27.5 cm along x,y,z. A light sheet (thickness $D_{\text{light}} = 5$ mm) illu-

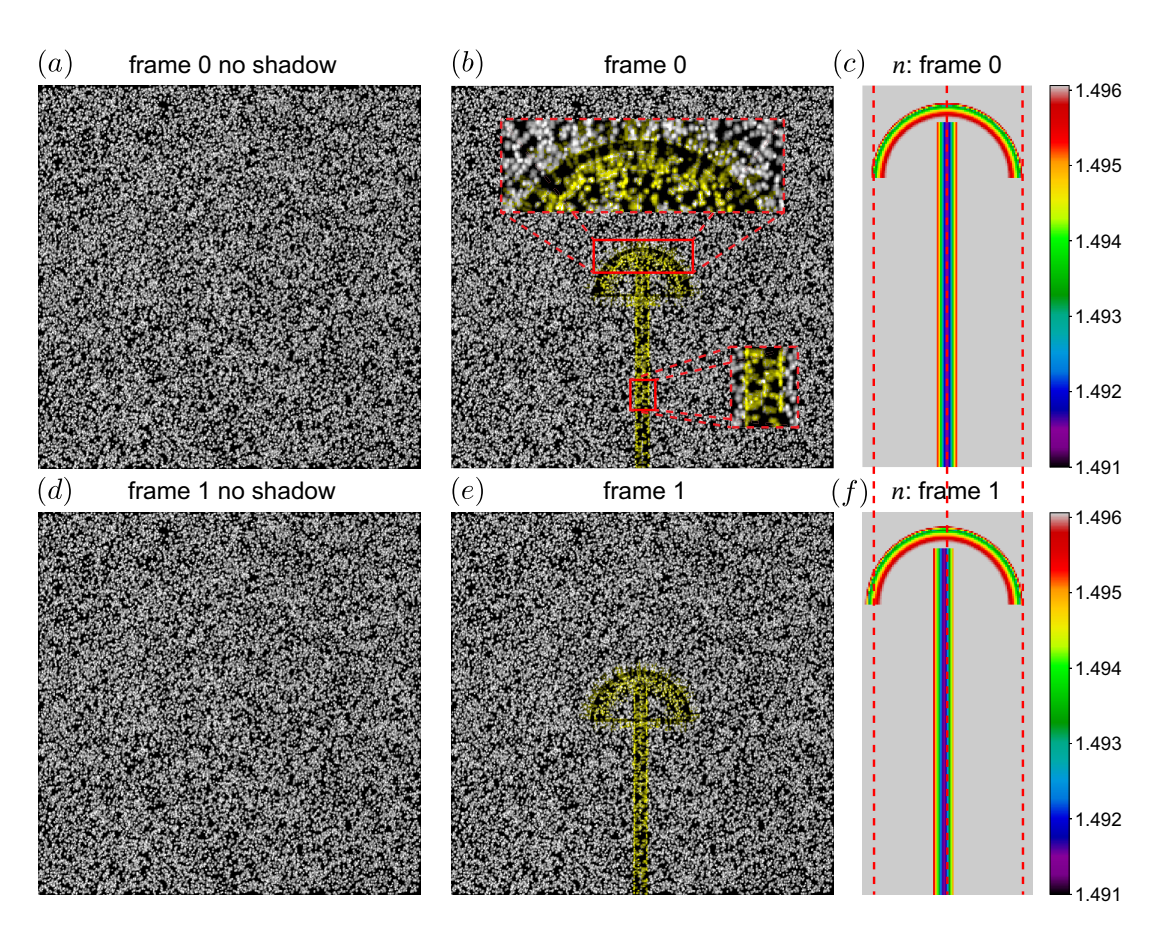


FIG. 7. Particle images and refractive index distribution in the synthetic test. (a) Particle image without the SA-PIVR at t_0 (frame 0). (b) Particle image with the SA-PIVR at t_0 SA-PIVR highlighted in yellow. Red dashed line rectangles are zoomed in from red solid line rectangles. (c) Central vertical cross section of the refractive index field n at t_0 . (d),(e),(f) as (a),(b),(c) for t_1 (frame 1). The SA-PIVR is highlighted in yellow in (b) and (e). Three reference lines (dashed red) are plotted across (c) and (f) to compare the size and position of the plume-like structure at t_0 and t_1 .

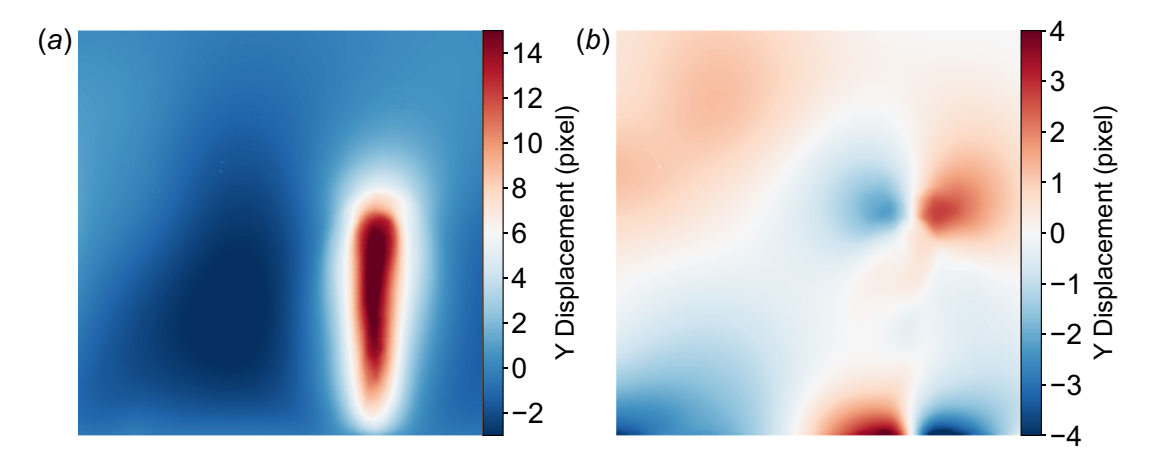


FIG. 8. Ground truth displacement used in the synthetic test. (a) Y displacement. (b) X displacement.

minates a plane within the test section, of which we simulate $_{425}$ a smaller inset (22.5 cm \times 22.5 cm). This smaller plane con- $_{426}$ tained in the original image just fits the image of $1024\times1024_{\scriptscriptstyle 427}$ pixels taken by a camera facing the center of the plane. $A_{\scriptscriptstyle 428}$ plume-like structure exists between the plane and the cam- $_{\scriptscriptstyle 429}$

420

421

422

423

era, at $Z_D=13$ cm from the illuminated plane. The working fluid has the same properties as the experimental fluid with $n_0=1.4961$ at ambient (reference) conditions (25 °C). To simplify the synthetic test and save computational cost, the ambient medium is set to be the same as the working fluid,

TABLE I. Comparison of the synthetic test and the laboratory experiment

	Synthetic	Experiment 40
working fluid	syrup	syrup 46
ambient medium	syrup $(n_0 = 1.4961)^a$	air $(n_0 = 1)^{46}$
$\left \frac{\delta n}{n}\right _{\text{max}}$	3.5 %	4.8 % 46
Z_D	13 cm	$0{\sim}40~{\rm cm}^{46}$
Z_A	227 cm	$68{\sim}107~\mathrm{cm}^{\mathrm{b}}$
f	171 mm	15 mm 46
Rhead	24 mm	10~100 mm 46
R_{stem}	3.6 mm	2.5~3.5 mm 46
R _{tracer}	$550\pm200~\mu m$	320±200 <mark>℃</mark> µm 47
$D_{ m light}$	5 mm	5 mm ₄₇
tracer density	7.3 per 16×16 pixels	7.3 per 16×16 pixels ₄₇
pixel size	0.22 mm	0.22 mm ₄₇
image size	1024×1024 pixels	
max Y displacement	15 pixels	25 pixels 4

 $[^]a$ at 25 $^{\circ} C$

431

433

434

437

438

440

441

442

443

444

445

447

449

450

452

453

455

458

459

instead of air (n=1) as in the experiment. To compensate for this simplifying assumption (c.f. Appendix \boxed{A}) and create particle images as similar to the experiment as possible, we use the same pixel size, and tracer density, but a larger Z_A , f and tracer size $R_{\rm tracer}$ (Table \boxed{I}). Fig. $\boxed{7}$ shows the final synthetic image used in the test.

2. Density gradient

We model a refractive index gradient zone with a volume of 491 60 mm \times 135 mm \times 60 mm along x, y, z centered at the plume-492 like structure (representing p_{if}), with a resolution of 0.6 mm⁴⁹³ for piece-wise linear ray tracing. This plume-like n anomaly⁴⁹⁴ consists of a cylindrical stem and half a spherical shell head₄₉₅ (cross section in Fig. 3c for frame 0). The cylinder has a ra-496 dius $R_{\text{stem}} = 3.6 \text{ mm}$, with a Gaussian $\left| \frac{\delta n}{n} \right|$ negative anomaly:497 a central peak of 3.5% and a half width at half maximum of 498 2.1 mm (or standard deviation $\sigma = 1.8$ mm). The spherical⁴⁹⁹ shell has an average radius of $R_{\text{head}} = 24$ mm, and a thick-500 ness of 6 mm, $\left|\frac{\delta n}{n}\right|$ which decays quadratically from 2.3% at 501 1/4 thickness from the top to 0 at the edge. These two simple geometrical components are designed to generate similar (actually stronger) tracer elongation in the particle images com-502 pared to the experiment (Fig. 2, 3). The synthetic particle images at frame 0 (t_0) with (and highlighted plume shadow)⁵⁰³ and without the density gradient are shown in Fig. 7a, b.504 The synthetic particle images are simulated using photon [31] photon is a Python-CUDA program that provides PIV/BOS⁵⁰⁵ image generation, powered by accurate non-linear ray tracing through density gradients using fourth-order Runge-Kutta schemes optimized for GPUs. More than a billion light rays507 are traced for each particle image.

3. Inter-frame flow

478

489

The in-plane flow for the synthetic images is taken from a numerical simulation with the same initial/boundary conditions and fluid properties as the experiment in Sec. [VI]. The numerical simulation is performed with the Finite Element package Firedrake [32]. The computational mesh is constructed with more than a half million unstructured tetrahedrons refined towards the bottom of the section.

For the ray tracing computation, we model the in-plane flow as 2D. We select a 22.5×22.5 cm region at a *z*-plane at a location and time close to those of the experiment. This plane contains a complete plume on the right and part of the root of another plume on the lower left corner (Fig. 8). We adopt a 2 s inter-frame delay, so the maximum displacement is 15 pixels along *y*. The tracers are then advected using the displacement in Fig. 8. The larger displacement of the synthetic test makes it more challenging to remove the SA-PIVR while preserving the in-plane plume flow, which makes it a more challenging test of the filter design.

We expand the average R_{head} by 4% from frame 0 (t_0) to frame 1 (t_1) for p_{if} . We also shift the entire structure 1 mm to the left, mimicking the behavior of a real growing p_{if} (Fig. 7). Fig. 7d and e show the synthetic particle images at t_1 with and without the density gradient.

Applying the CCPIV algorithm along with WiDIM and a median filter, to the synthetic particle image pairs with a p_{if} , we find an obvious SA-PIVR at the center of the image (Fig. 9a) with a thickness comparable to those in the experiment (Fig. 2d) and about half of the plume core thickness.

B. Filtering of the synthetic data

Fig. 9 shows the filter applied to the synthetic PIV lateral displacement results. PIV results without density gradients are shown in Fig. 10a,d for comparison. The binary mask covering the plume core (green dashed line boxes) and the SA-PIVR (red dashed line box) constructed using the non-local means filter (corresponding to Fig. 4d) is shown in Fig. 9b. Both are captured accurately. To remove the SA-PIVR from the mask, we apply morphological opening (Fig. 9c). The plume core is overall unchanged. The final filtered CCPIV result can be found in Fig. 9d. For completeness, we also present the raw CCPIV result with the SA-PIVR and the filtered version for the vertical displacement in Fig. 10b,c.

C. Quality assessment of the filtered PIV results

Below we combine qualitative and quantitative evaluation of the PIV plume filter using the following criteria:

- 1. Remove the SA-PIVR effectively.
- 2. Preserve the strength of the in-plane plume flow.
- 3. Maintain the overall flow pattern (in the spatial and spectral domains)

 $^{^{\}rm b}$ $Z_D + Z_A = 107$ cm

^c apparent size; actual size $15\pm1.5~\mu m$

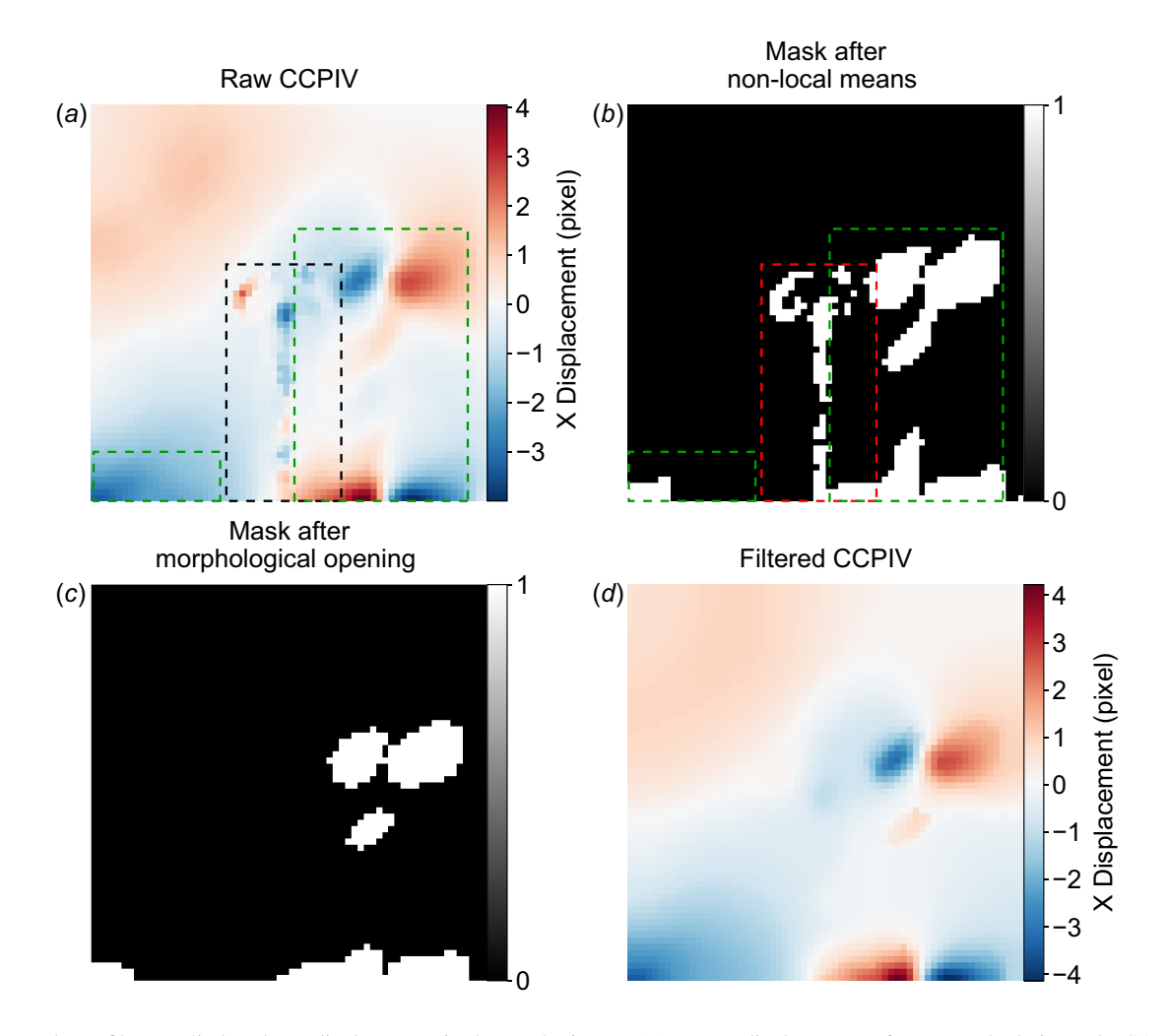


FIG. 9. PIV plume filter applied to the X displacement in the synthetic test. (a) Raw X displacement after PIV calculation. The SA-PIVR and the in-plane plume are bounded by black and green dashed line boxes, respectively. (b) Binary mask containing both the plume core region and SA-PIVR. Boxes as in (a). (c) Mask after applying morphological opening to (b). (d) Final X displacement after applying the PIV plume filter.

1. Qualitative assessment

We start with visual inspection of the result. Before the fil-526 tering, the visually distinct SA-PIVR is located in the center527 (black dashed line box in Fig. 9a); after the filtering, no ob-528 vious anomalous lateral displacement can be seen within the same area of the image (Fig. 9d). The lateral displacement of the plume core (within the green dashed line boxes in Fig. 9a) is consistent in shape and amplitude before and after the 529 filtering (Fig. 9d). The large-scale in-plane flow is overall untouched (e.g., interface between the red and blue dashed line 530 rectangles in Fig. 9a, d). This is also true for the vertical displacement (10b,c). The filter passes the qualitative evaluation. 532

2. Quantitative assessment

To objectively assess the quality of the proposed filter, we use several different metrics to compare the raw and filtered

PIV results against the PIV without a density gradient (or *n* anomaly) and therefore no shadow. First, we use the Root Mean Squared Error (RMSE) as one of the main error indicators. RMSE is the square root of the mean of the squared Euclidean distances between two vectors:

RMSE =
$$\sqrt{\frac{1}{N} \sum_{i=1}^{N} ||u_i - u_{0,i}||^2}$$
. (14)

where u_i is the displacement at the *i*-th point, u_0 is the PIV result in the absence of a plume shadow, and N represents the number of vectors.

A variant of RMSE called Average Endpoint Error (AEE) directly uses the mean of the Euclidean distances (or endpoint errors):

$$AEE = \frac{1}{N} \sum_{i=1}^{N} \| \boldsymbol{u}_i - \boldsymbol{u}_{0,i} \|.$$
 (15)

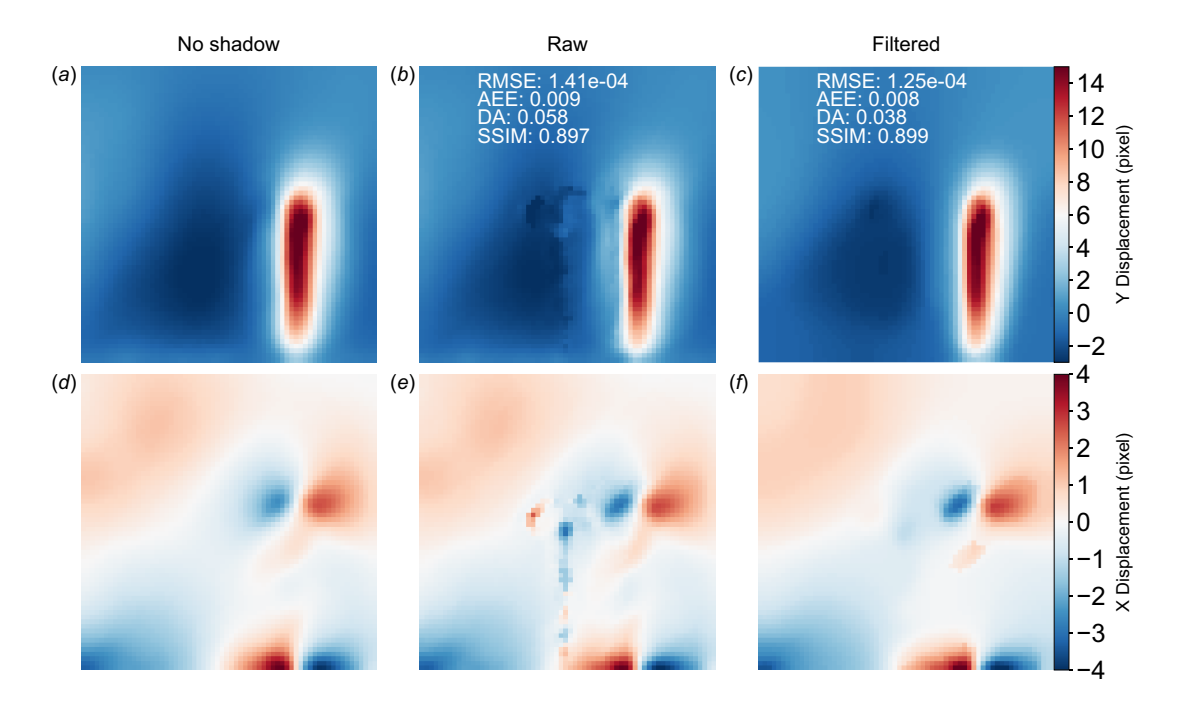


FIG. 10. (Top) PIV of the synthetic image before and after filtering. (a) PIV without SA-PIVR. (b) Unfiltered (raw) PIV result if SA-PIVR present. (c) PIV after filtering applied to (b). (Bottom) Error metrics averaged over two components of the PIV vector compared to the synthetic ground truth in (a). Lower values are higher quality, except for SSIM. (d) RMSE: root mean square error. (e) AEE: Average Endpoint Error. (f) DA: Dissimilar Area. SSIM: Structural Similarity Index Measure.

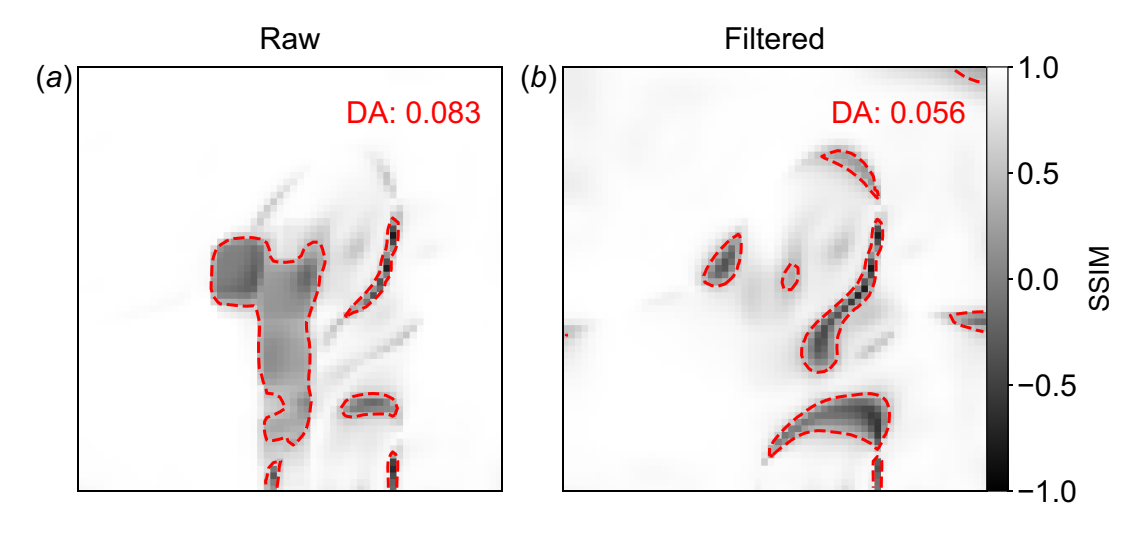


FIG. 11. Map of Structural Similarity Index Measure (SSIM) of (a) Raw PIV result and (b) filtered result for the X displacement in the synthetic test. DA: Dissimilar Area, relative ratio of number of pixels with SSIM < 0.5 over that of the total pixels.

Compared with RMSE, AEE is less sensitive to large out-547 liers because outliers are weighted less. For the in-plane flow,548 RMSE focuses more on the plume core (larger displacements are prone to larger error), while AEE is more representative of the contribution from the large-scale flow with smaller dis-549 placements. For the SA-PIVR, the error will usually be large, and the contribution from SA-PIVR will be larger for RMSE. 550

538

539

541

542

543

545

546

The Structural Similarity Index Measure (SSIM)³³ is a₅₅₁ great candidate for measuring the differences in the neighbor-₅₅₂ hood of a PIV vector between two results, as well as differ-₅₅₃

ences in the PIV vector itself. It is therefore ideal for assessing the quality of the SA-PIVR filter removal. It is defined as:

$$SSIM(i) = \frac{(2\mu_u\mu_{u_0} + C_1)(2\sigma_{uu_0} + C_2)}{(\mu_u^2 + \mu_{u_0}^2 + C_1)(\sigma_u^2 + \sigma_{u_0}^2 + C_2)} \text{ for } \mathcal{B}(i). (16)$$

where $\mathcal{B}(i)$ is a 7×7 window centered at vector i, μ_u is the mean displacement within $\mathcal{B}(i)$, σ_u the corresponding variances. The subscript u refers to the PIV result to be checked, and u_0 the PIV result in the absence of a plume shadow. σ_{uu_0}

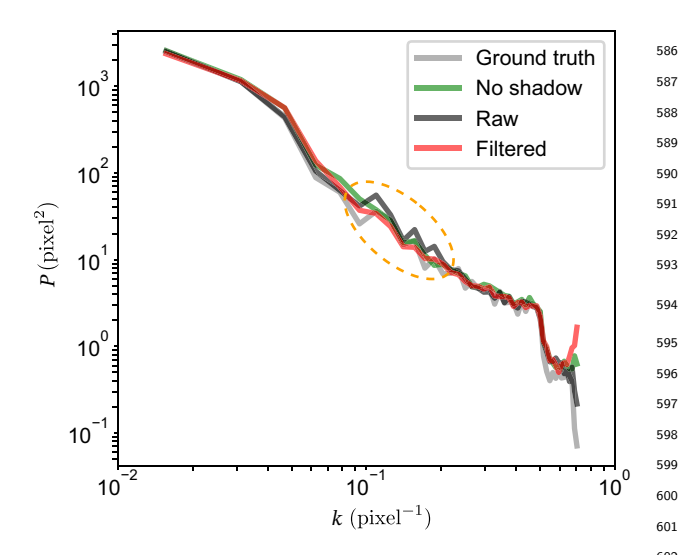


FIG. 12. Power Spectral Density (PSD) of the displacement vector₆₀₃ of the synthetic test. Gray: ground truth from Fig. 8 Green: CCPIV₆₀₄ with no shadow. Black: raw CCPIV with shadow. Red: filtered₆₀₅ CCPIV with shadow. Dashed yellow oval highlights the frequency₆₀₆ to which the SA-PIVR contributes.

is the covariance. C_1 and C_2 are constants to stabilize the di-⁶⁰⁹ vision with a weak denominator. SSIM for different compo-⁶¹⁰ nents (u_x, u_y) is computed separately. A final SSIM can be⁶¹¹ obtained by averaging the SSIM map from Eq. [16] over both⁶¹² components at all points. SSIM ranges from 1 (perfect match)⁶¹³ to -1 (completely unmatched).

554

555

557

559

560

562

563

564

566

567

569

570

572

573

575

578

579

581

584

Finally, based on the SSIM map, we introduce a new metric 615 called Dissimilar Area (DA):

$$DA = \frac{\sum_{i=1}^{N} \mathbb{I}(SSIM(i) < 0.5)}{N}.$$
 (17)₆₁₇

where \mathbb{I} is an indicator function that is either 1 (if the condi- $_{618}$ tion is true) or 0 if false. DA provides the relative area of the dissimilar region. Compared with SSIM, DA offers a metric $_{619}$ on the similarity of the planforms of the PIV results affected or unaffected by the plume shadow.

The four error metrics for the raw CCPIV and the filtered results compared to the PIV when a density gradient is present are summarized in Fig. 10. Lower values represent a higher quality result except for SSIM, for which the opposite is true. The filtered version is significantly and systematically better than the pre-filtered version. Both RMSE and AEE drop by⁶²⁴ 11% after filtering. The average SSIM is only marginally higher with our filter (due to the small total area of the SA-PIVR), but DA decreases by 34%. To illustrate the improve-625 ments due to the filter, we further show the SSIM map for 626 the lateral displacement in Fig. [11] with a SSIM=0.5 con-627 tour plotted as red dashed lines. The raw CCPIV result con-628 tains a large dissimilar patch in the center due to the SA-PIVR⁶²⁹ (Fig. 11a), which almost completely vanishes after the filtering (Fig. 11b). Taken together these metrics suggest that the⁶³⁰ SA-PIVR filter can largely eliminate the SA-PIVR while retaining the pattern and amplitude of the fast in-plane flow due631 to plumes.

In addition to the error metrics above, we also inspect the frequency-dependent flow distribution by computing the Power Spectral Density (PSD). We apply a 2D Fourier transform to the lateral and vertical displacements as the real and imaginary parts $u_x + ju_y$. In this way, both components can be included at the same time (the order of u_x and u_y does not matter). If the x and y dimensions do not agree (as in the experiment), we scale x to y in frequency. We obtain a 1D PSD by binning data radially (along $\sqrt{k_x^2 + k_y^2}$, where k is the wave vector) in the 2D spectral domain.

PSD P(k) at different wave vectors k is plotted in Fig. 12 for the ground truth, i.e., the synthetic PIV results for the flow in the absence of shadows cast by plumes in front of the illuminated plane of interest, in the presence of shadows, and after filtering. P(k) of the raw CCPIV result is characterized by a few peaks at $k \sim 0.1$ to 0.2, much higher (up to 60%) higher) than that of the ground truth or the SA-PIVR (within the dashed oval in Fig. 12). This could be mistakenly interpreted as the existence of a vigorous flow at smaller scales than the in-plane plume flow. After the filtering (red line in Fig. 12), P(k) reduces to levels similar to those of the PIV not affected by shadows, and the two curves (red and green) are largely consistent. The only exception is at the highest k, an anomalous peak appears in the filtered result, which is likely a by-product of stitching (Fig. 4f,g,h). Nevertheless, this peak contributes only negligibly to the PSD.

The synthetic test shows that the PIV plume filter preserves the in-plane flow strength in the spatial and spectral domains and removes the SA-PIVR as defined in our original goals. Most importantly after filtering the PIV results are as satisfactory as if no density gradient were present.

VI. APPLICATION TO EXPERIMENTAL DATA

A. Experiments in Viscous Fluids

1. Thermal Convection in Viscous Fluids

In viscous fluids, the strength of the convective flow and its time dependence can be represented by the global Rayleigh number *Ra*, which describes the ratio of the diffusive over convective time-scales for heat transport. *Ra* is defined as:

$$Ra = \frac{\tau_{\text{diff}}}{\tau_{\text{conv}}} = \frac{H^2/\kappa}{\frac{H}{\rho \alpha \Delta T g H^2/\eta}} = \frac{\rho g \alpha \Delta T H^3}{\eta \kappa}$$
(18)

where ρ is the reference density, g is gravity, α thermal expansivity, ΔT , the temperature difference driving the flow, H is the thickness of the convective region, η , the viscosity and κ , the thermal diffusivity.

The effect of inertia is described by the Prandtl number Pr:

$$Pr = \frac{\eta/\rho}{\kappa} = \frac{\nu}{\kappa} \tag{19}$$

, where *v* is the kinematic viscosity. For viscous enough fluids (Pr>1000), the effect of inertia is essentially negligible $\frac{34}{2}$.

2. Experimental setup

We conducted a thermal convection experiment with basal heating in a very viscous fluid (Pr > 3000) undergoing vigorous convection ($Ra = 1.9 \times 10^6$, while the critical Rayleigh number is $Ra_c = 1708^{\frac{35}{35}}$) dominated by plumes. The goal of the experiment was to study the collective dynamics and morphological evolution of plumes applicable to Earth's interior. We used scanning stereoscopic PIV to acquire 3D velocity over time, covering the clusters of plumes in the fluid domain. The plumes frequently cast shadows on the illuminated planes and corrupted the PIV results.

3. Test section and initial/boundary condition

The test section has internal dimensions of $40 \text{ cm} \times 40 \text{ cm}^{679} \times 27.5 \text{ cm}$ along x,y,z. It is made of 1 cm thick acrylic walls with a refractive index nearly identical to that of the working⁶⁸⁰ fluid (~ 1.49) and low thermal diffusivity ($10^{-7} \text{ m}^2/\text{s}$) effec-⁶⁸¹ tively insulating the sides. The tank has an aluminum top lid⁶⁸² and an aluminum false bottom. The lid of the tank was kept at⁶⁸³ room temperature ($25 \,^{\circ}\text{C}$), while the false bottom of the tank⁶⁸⁴ was heated ($80 \,^{\circ}\text{C}$) with a silicone heating mat controlled by⁶⁸⁵ a PID controller. The heater was turned on at $t=0 \, \text{s}$, and⁶⁸⁶ the temperature of the bottom increased nearly linearly from⁶⁸⁷ $25 \,^{\circ}\text{C}$ to $80 \,^{\circ}\text{C}$ in $250 \, \text{s}$. The bottom temperature thence re-⁶⁸⁸ mained constant until the end of the experiment ($\sim 8000 \, \text{s}$).⁶⁸⁹ The ambient medium outside the tank is air.

4. Working fluid

The working fluid was Gateway Du-Crose 3 63/43 corn⁶⁹⁵ syrup, clear and chemically stable, characterized by high and⁶⁹⁶ strongly temperature-dependent viscosity. Its slight super-⁶⁹⁷ exponential temperature dependency was measured with an⁶⁹⁸ Ametek Brookfield DV2TLV viscometer and is given by: ⁶⁹⁹

$$\eta = \exp(4.642 \times 10^{-4} T^2 - 1.246 \times 10^{-1} T + 6.325). (20)_{701}^{700}$$

Here T is in ${}^{\circ}$ C, η is in Pa·s. With temperatures between 25 to⁷⁰² 80 ${}^{\circ}$ C the maximum viscosity contrast ($\gamma = \eta_{\text{max}}/\eta_{\text{min}}$) was⁷⁰³ 65.

The refractive index n was obtained using a Hanna instru-705 ments refractometer HI96800 and is given by:

$$n = -2.058 \times 10^{-4} T + 1.5012. \tag{21}_{709}^{708}$$

The temperature dependence of the density ρ (in kg/m³)₇₁₀ was measured with a Cole-Parmer Specific Gravity Hydrom-₇₁₁ eter Set as:

$$\rho = -5.875 \times 10^{-1} T + 1442. \tag{22}$$

The Gladstone-Dale constant K was determined with Fig. 9, 21, 22 to be $K = 3.5 \times 10^{-4}$ m³/kg.

Table II summarizes all the properties of the fluid measured₇₁₈ in the lab or obtained from the manufacturer.

Properties	Symbol	Value
Density	ρ	1427 kg/m^3
Dynamic viscosity	η	33.1 Pa·s
Kinematic viscosity	v	$0.023 \text{ m}^2/\text{s}$
Index of refraction	n	1.4961
Thermal expansion coefficient	α	$4.1 \times 10^{-4} \text{K}^{-1}$
Thermal conductivity	k	$0.346 \text{ W} \cdot \text{m}^{-1} \text{K} - 1$
Specific heat capacity	C_P	2300 J/kg·K
Thermal diffusivity	$\kappa = k/(\rho C_P)$	$1.05 \times 10^{-7} \text{ m}^2/\text{s}$
Prandtl number	$Pr = v/\kappa$	2.2×10^{5}

TABLE II. Corn syrup properties at 25°C. C_P and k are from the manufacturer.

5. Stereoscopic Scanning PIV system

Different from Fig. [1] we used a 3D Scanning Stereoscopic PIV system (Fig. [13]). The test section sits on an Newport RPR-510-12 optical table. Two JAI AT-200 CL CCD RGB cameras (1620 × 1236 pixel resolution) with Fujinon TF15DA-8 15 mm lenses, with a separation angle of 17.8° are mounted on a movable arm, at the height of the center of the test section. A white LED light source (Hecho S5000 with up to 572 000lx luminance) is connected to a Volpi fiber optic lightline with a cylindrical lens (300 mm length, 13.1 mm diameter). A 305 mm by 15 mm Fresnel lens (51mm focal length) is mounted in front of the cylindrical lens to produce a non-divergent thin (5mm) light sheet illuminating a plane section of the fluid. The distance from the light plane to the cameras is 107 cm. The stereoscopic arrangement captures the out-of-plane velocity.

The cameras and the lightline are mounted on motion-controlled linear slides with pitched screws, connected to Applied Motion Products' stepper motors HT34-489D-YAA with 1.8° step angle, powered by Applied Motion Products' Stac6-Si drives within a controller. The data acquisition process involves synchronously and simultaneously driving the cameras and the lightline using separate stepper motors, controlled by signals from the controller.

We use Potters Conduct-O-Fil SP30S20 silver-coated polymer spheres as tracer particles (30 ppm, or 2 g for the whole fluid volume). This tracer is neutrally buoyant (density 1487 kg/m³), highly reflective with a radius distribution of 15 \pm 1.5 $\it mu$ m. Due to the finite thickness of the light plane (layers of tracers collapsed into a 2D image), possible tracer agglomeration, and the refraction at the tank-air interface, the apparent tracer size determined from the particle images is much larger (320 \pm 220 μ m), which permits the optical elongation of tracers.

For this paper, we show only 2D in-plane flow. The particle images from the camera on the left were dewarped (now 1837×1247 pixels resolution) as if the camera were facing the middle of the tank (i.e., the line of the sight and the tank are perpendicular). The particle images (Fig. 2a, 3a,b) were taken at t = 704 s with an inter-frame delay of 1.5 s. The location of this plane (along z) is 7 cm from the center of the tank

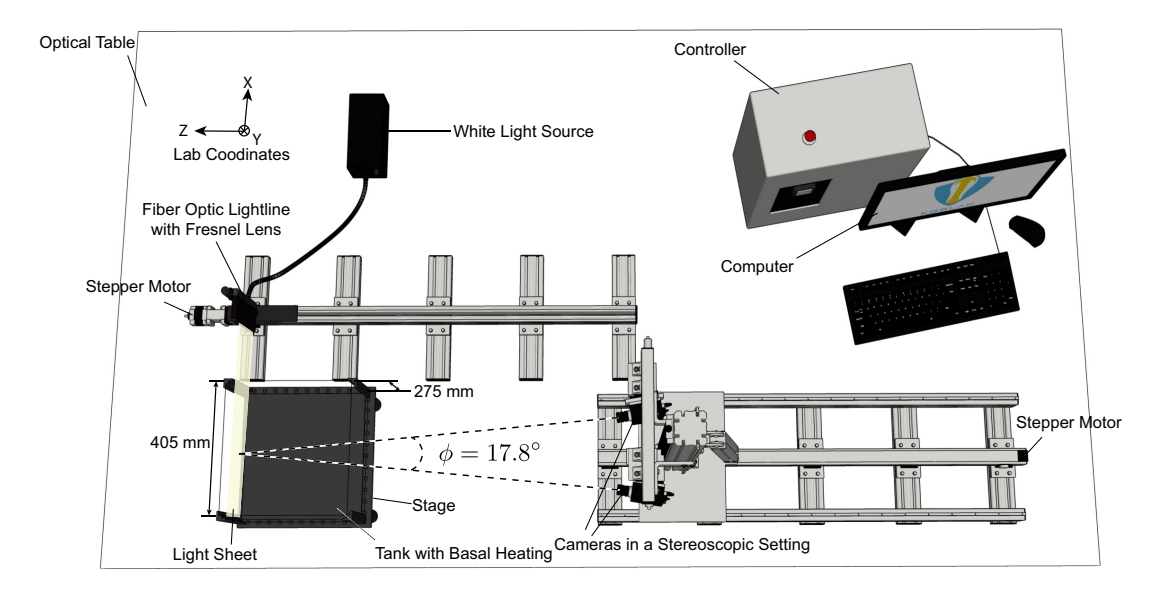


FIG. 13. Experimental setup for the 3-D scanning, Stereoscopic, Particle Image Velocimetry system. The bottom and lid (not shown) of the tank are made of aluminum. The lightline (therefore light sheet) and cameras can move simultaneously, driven by the stepper motor controlled by the controller and the computer.

758

away from the cameras.

722

723

725

727

728

729

731

732

733

734

735

737

738

740

741

743

744

746

747

749

750

The $\left|\frac{\delta n}{n}\right|_{\text{max}}$ is estimated using the numerical simulation⁷⁵² (c.f. Sec. \boxed{V}) and a typical plume stem center temperature of⁷⁵³ ~ 60 °C. The size of the plume head/stem is estimated from⁷⁵⁴ Fig. $\boxed{2}$ c. Other details of the experiment are summarized in⁷⁵⁵ Table $\boxed{1}$ l

B. Filtering of the experimental PIV data

Compared to the simple synthetic PIV case with 1 p_{ip} and 761 1 p_{if} , the experimental raw data show 2 p_{ip} and at least 7 p_{if}^{762} (Fig. 2).

For the lateral displacement, the mask created with nonlocal means picks up both the SA-PIVR (black or red dashed 765 line rectangles) and the plume core (green dashed line rectangles) regions, as desired (Fig. 14a,b). As we apply the 767 morphological opening, the majority of the SA-PIVR is re-768 moved from the mask. Only very small patches are left (cyan dashed line rectangles), while the plume core region is mostly preserved (Fig. 14c). Subsequent operations, especially the 769 final non-local means smoothing after stitching (Fig. 4f,g,h,i), make the contribution of the leftover SA-PIVR (Fig. 14c) neg-770 ligible (Fig. 14d), while the amplitude of the displacement in the plume core and overall flow pattern are maintained. The771 filtering applied to the vertical displacement also yields the de-772 sired result (Fig. 15). There are some left over regions of SA-773 PIVR in the final mask (Fig. 15c), which have an area larger774 than that for the lateral displacement (Fig. 14c). However,775 these regions mostly cover areas dominated by the smooth in-776 plane flow, not SA-PIVR (leftmost and rightmost evan dashed777 line rectangles in Fig. 15c). They are included in the mask₇₇₈ because they are in the vicinity of the SA-PIVR. The filtered₇₇₉ end results still contain the two strong upwellings (up to 25₇₈₀

pixels displacement) and the large-scale flow pattern, and no visible SA-PIVR.

Although none of the error metrics in Sec. ∇ can be computed for the experiment, we can still compare the PSD before and after the filtering (Fig. 16). P(k) of the filtered result (red) is systematically smaller than that from the raw CCPIV result (black) for a broad frequency range (k > 0.08, yellow oval). This is consistent with the PSD comparison with the synthetic case (Fig. 12), while the broader frequency range of smaller powers after filtering seen here is likely due to the presence of many more p_{if} in the real experiment (7 instead of 1 in the synthetic test).

Taken together, the proposed filter is still effective on real life experimental data. Applied to PIV results without any SA-PIVRs, it preserves the in-plane flow pattern. This post-processing filter costs ~ 1 s of computational time. Therefore, it can be adopted for all the data in an experiment. It does not interfere with the normal PIV interrogation, but enhances it.

C. Discussion

1. Using the SA-PIVR to measure plume morphology

Up to now we have tried to eliminate the effects of the shadow casts by plumes. However, the SA-PIVR is not just a nuisance. Similar to BOS that can be used to construct the density gradient distribution, the SA-PIVR is useful for understanding the location, size, morphology and evolution of plumes (including the radius of the plume head and stem in Table [I]). The dense velocity estimates from optical flow are particular useful here because the extent of the SA-PIVR can be determined with pixel-level accuracy (Fig. 2c). Since the optical displacement is sensitive to large $|\nabla n|$, the SA-PIVR

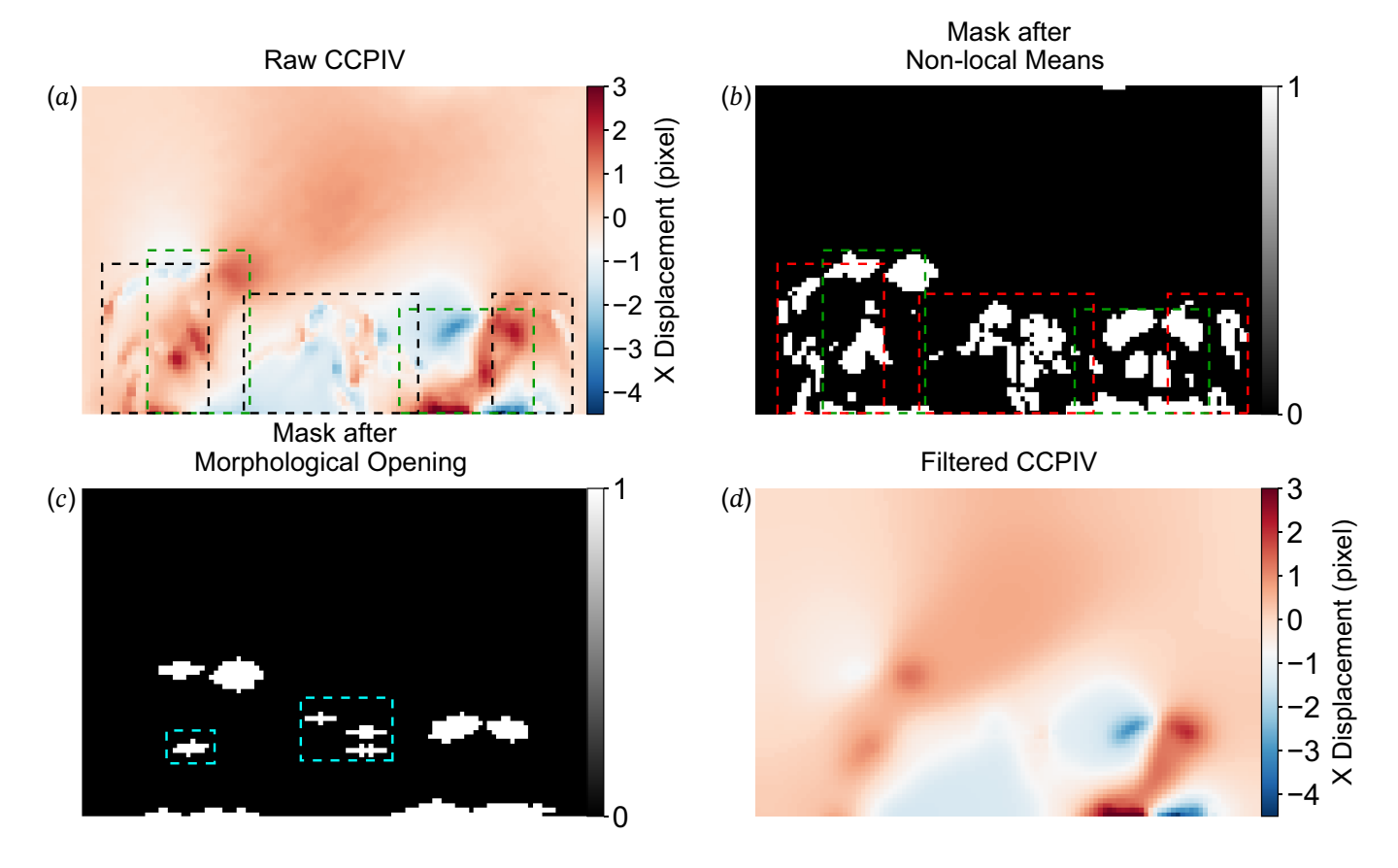


FIG. 14. PIV plume filter applied to the X displacement data from the laboratory experiment. (a) X displacement from CCPIV. SA-PIVRs and in-plane plumes bounded by black and green dashed line boxes, respectively. (b) Mask after non-local means containing both the plume core and the SA-PIVR. Boxes as in (a). (c) Mask after applying with morphological opening to (b). (d) Final filtered X displacement.

is inherently consistent with material surfaces at the edge of $_{803}$ plumes tracked by Lagrangian analysis like Finite-Time Lya- $_{804}$ punov Exponent (FTLE) $_{30}^{30}$. As a result, the SA-PIVR can- $_{805}$ be used as a benchmark on plume morphology from the PIV- $_{806}$ experimental measurements and its digital twin. The optical- $_{807}$ distortion in the particle image, including the elongation of $_{808}$ tracers (Fig. $_{2a}$,b, Fig. $_{3a}$,b), can be compared against simu- $_{809}$ lated particle images (e.g., Fig. $_{10}$), a more direct proxy for $_{810}$ $_{10}$ vn itself. The scanning, stereoscopic nature of our PIV setup offers many more possibilities, since the particle images of each plane provide information of the $_{1p}$ and $_{1f}$ at different $_{11}$ times. The 4D velocity obtained enables the calculation of the FTLE field, the tracking of Lagrangian Coherent Structures $_{11}^{37}$ defining the plumes, which can then be compared with the $_{11}$ SA-PIVR bands $_{12}^{6}$.

2. Applicability to other scenarios

Our PIV plume filter can be easily tuned for other laminar₈₁₉ flow experiments with visually distinct optical distortion ef-₈₂₀ fects. It will be applicable as long as the length scale of the₈₂₁ distortion effect is smaller than the typical length scale of the₈₂₂ in-plane flow. The only input needed for the tuning are a few₈₂₃ pairs of images. Indeed, our filter is suitable for any displace-₈₂₄

ment measurement with two or more visually distinct features characterized by different length scales. For example, laminar flow with missing data due to obstruction of thin objects. It can be used for general denoising purposes, thanks to the embedded non-local means filter. The tracer elongation due to the large (effective) tracer size and high ∇n makes the distortion harder to remove in our case, therefore our filter should work even better in the absence of the elongation.

VII. CONCLUSIONS

We presented an algorithm to mitigate a common issue in PIV: optical distortion due to density gradients in the fluid itself. We focused on visually distinct anomalous PIV vectors in viscous thermal convection with plumes and analyzed the difference between the in-plane flow and the contribution from the optical distortion in PIV results from a laboratory experiment. The proposed PIV plume filter is based on a series of conventional image processing tools including non-local means denoising and morphological opening. This filter is designed to extract the domain affected by the optical distortion (SA-PIVR) and the fast in-plane flow related to plumes (plume core) in the PIV. It creates a mask that removes the SA-PIVR and only contains the plume core.

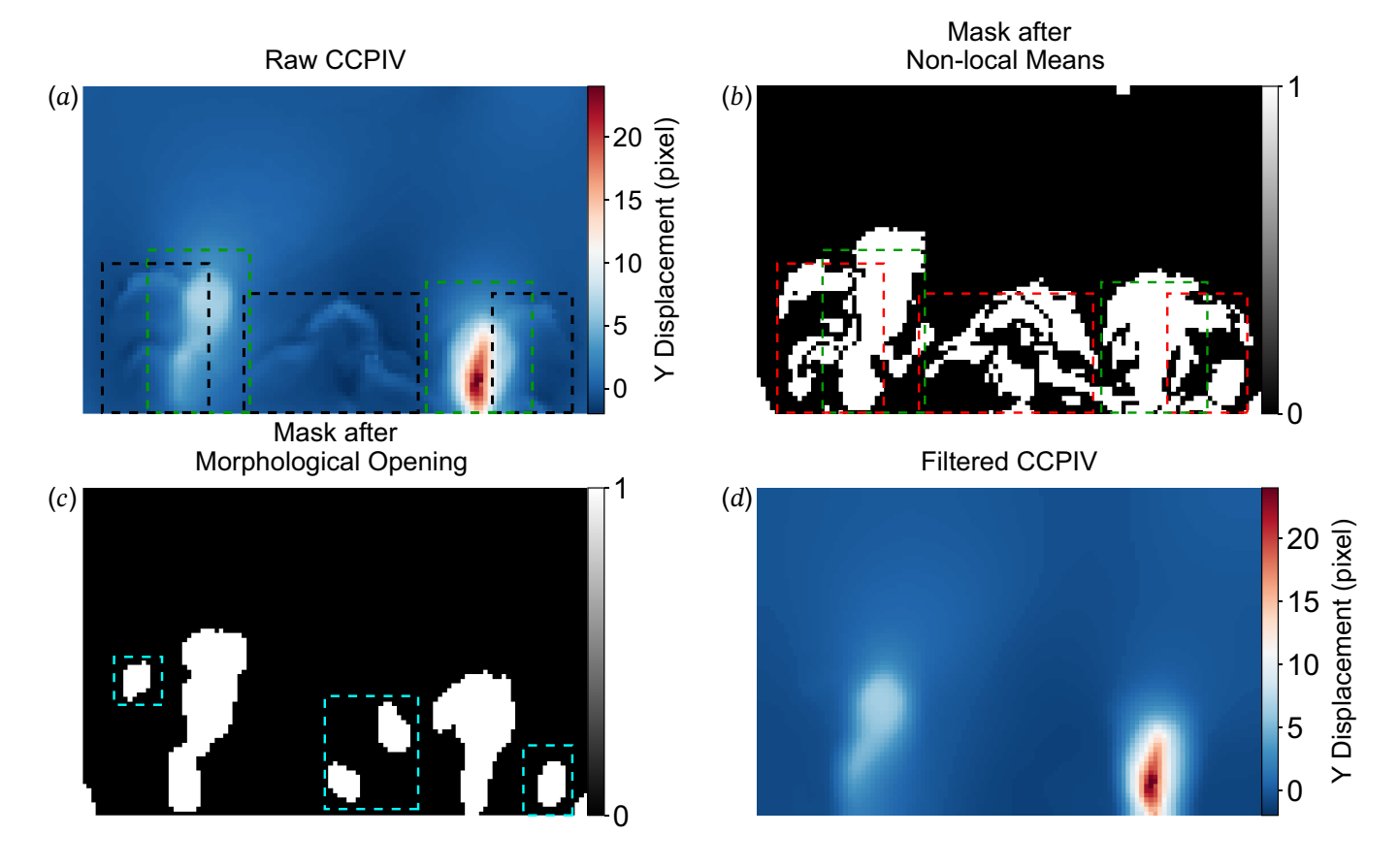


FIG. 15. Y displacement. Panels as in Fig. 14

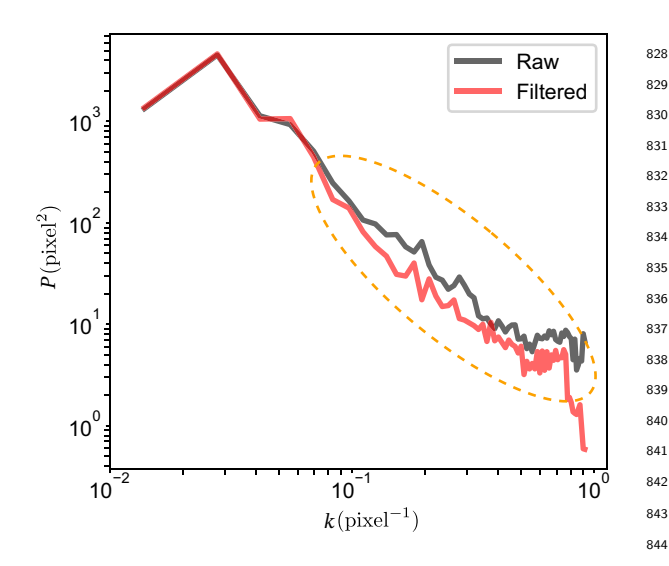


FIG. 16. Power Spectral Density (PSD) of the displacement vectors⁸⁴⁵ for the laboratory experiment. Raw shadow affected CCPIV (black⁸⁴⁶ line) and filtered CCPIV (red line) results. The dashed yellow oval⁸⁴⁷ highlights the contribution of the SA-PIVR.

A synthetic test shows the filter performs well. In the852 test, light rays scattered from particles in an illuminated plane853 travel through the density and refractive index gradient con-854

826

827

taining a plume-like structure, exit the working fluid, enter the ambient medium, and finally hit the lens and sensor of the camera. The in-plane flow velocity was taken from a numerical simulation replicating a laboratory experiment with a high Ra fluid (corn syrup) heated from below. Synthetic particle images were created by tracking billions of light rays using the photon on GPUs, and PIV results with and without the density gradient were obtained. We compared the filtered and unfiltered PIV results against the version without any density gradient qualitatively and quantitatively. In the quantitative assessment, four error metrics (RMSE, AEE, SSIM, DA) were calculated along with the PSD. We find that the filtered PIV is systematically better than the unfiltered version, and our goals to remove the SA-PIVR, preserve the in-plane plume strength and the overall flow pattern were fulfilled.

We applied the PIV plume filter to a laboratory experiment. Over 60 kg of corn syrup was heated from below and cooled from above for 8000 s, at a $Ra = 1.9 \times 10^6$ and a $Pr \geq 3.4 \times 10^3$. The vigorous flow was effectively inertiafree and dominated by plumes. We use a bespoke 3D scanning stereoscopic PIV system to obtain flow velocities. For the purposes of this study we focus only on its equivalent 2D result in one plane. For the examined plane, at least 7 plumes were in front of the illuminated plane, casting shadows on the raw image and creating significant bands of SA-PIVR. There were at least two in-plane plumes. Despite of the more challenging conditions, the proposed filter successfully removed the SA-

PIVR bands and kept the in-plane flow largely untouched.

Compared with in principle more sophisticated, end-to-end approaches with deep learning, our filter is fast, robust, and does not require ray tracing or a large training dataset. Given its effectiveness and efficiency, this filter could be used as a baseline method to be compared with other approaches. Our PIV plume filter can be used not only for removing the distinct optical distortion effects in laminar flow, but also to fill missing flow measurements and for general denoising purposes. Finally, the optical distortion cast by the plumes in the particle image and PIV results can be directly used to estimate the plume morphology and geometry and serve as a benchmark for the integrated 4D PIV experimental results or their digital twins through Lagrangian analysis.

869 ACKNOWLEDGMENTS

855

856

857

858

859

860

862

865

866

867

868

870

871

873

876

879

880

881

882

884

885

886

887

888

890

891

894

897

899

900

901

This project is supported by the National Science Foundation under grant EAR-1900633 to CLB. CLB was also supported by the Louis B. and Martha B. Slichter Endowed Chair in Geosciences.

DATA AVAILABILITY STATEMENT

The data that support the findings of this study are openly available at https://doi.org/10.5281/zenodo.13334031.

Appendix A: Camera in the syrup approximation

In the ray tracing code photon only light rays with angles that connect the source point (tracer) and the camera (aperture-lens-sensor) will be modeled, which saves computational cost (yellow highlighted area in Fig. [17]). However, 903 when the working fluid is syrup (n > 1.49) and the ambient⁹⁰⁴ medium is air (n = 1), a light ray may undergo total reflection, if the source point is not at the center (dashed line and dotted arrow in Fig. [17]. In contrast, a light ray from the same⁹⁰⁵ source point (green arrow) could hit the camera sensor, with 906 an angle outside of those covered in the ray tracing. Even if $\frac{1}{900}$ we change the code to solve this issue, we will still need to₉₀₉ expand the modeled density gradient volume from the region⁹¹⁰ of interest (60 mm $\times 135$ mm $\times 60$ mm) to a much larger re- 911 gion (at least 400 mm \times 275 mm \times 180 mm) that covers the $_{913}^{912}$ entire syrup-air interface. To save the computational cost, we instead approximate the camera in the air (camera 0) with a₉₁₅ camera in the syrup (camera 1, Fig. 17). By moving the cam-916 era further from the test section, we can still capture the light 917 from the source point at the camera sensor (dashed-dotted arrow). To fit the particle image into the sensor, the focal length₉₂₀ of the lens will need to be larger; tracers also need to be larger921 to compensate for the longer object distance $(Z_A + Z_D)$, while 922 Z_D is fixed). The longer object distance leads to longer tracer⁹²³ elongation with the same ∇n , so a smaller $|\frac{\delta n}{n_{\max}}|$ than that $_{925}^{924}$ of the experiment is needed. These parameters $(Z_A, f, R_{\text{tracer}}, _{926}^{924})$

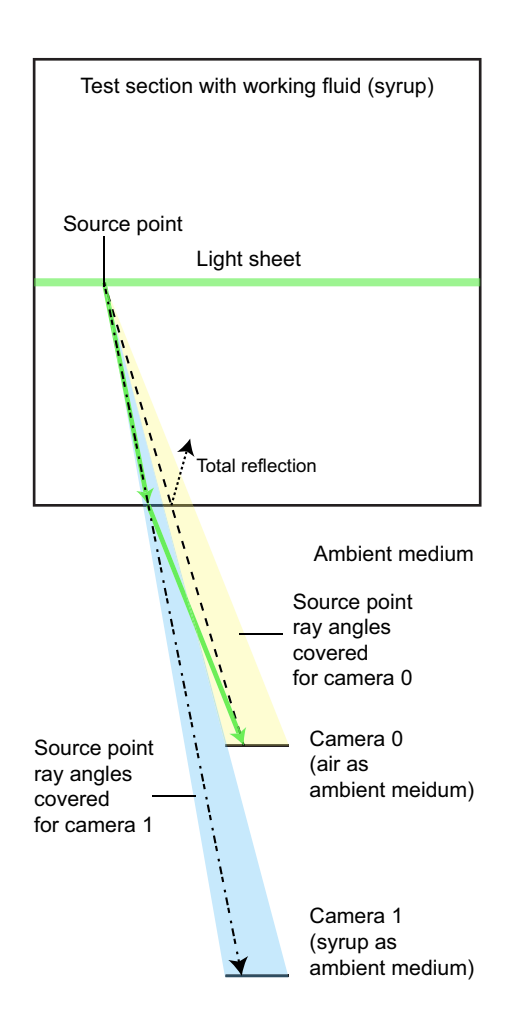


FIG. 17. Schematic illustration of how the camera in the air at position 0 is approximated with camera in the syrup at position 1.

 $\left|\frac{\delta n}{n_{\max}}\right|$) are adjusted to have similar effective tracer size and elongation as the experiment (Table []).

¹R. J. Adrian, "Twenty years of particle image velocimetry," Experiments in fluids **39**, 159–169 (2005).

²G. E. Elsinga, B. W. van Oudheusden, and F. Scarano, "Evaluation of aero-optical distortion effects in piv," Experiments in fluids 39, 246–256 (2005).

³F. Scarano, "Overview of piv in supersonic flows," Particle Image Velocimetry: New Developments and Recent Applications , 445–463 (2007). ⁴V. Valori, G. E. Elsinga, M. Rohde, J. Westerweel, and T. H. van Der Hamer ("Device in the control of the control o

y, valori, G. E. Eisinga, M. Konde, J. Westerweet, and T. H. Van Der Hagen, "Particle image velocimetry measurements of a thermally convective supercritical fluid," Experiments in Fluids **60**, 1–14 (2019).

⁵S. Androvandi, A. Davaille, A. Limare, A. Foucquier, and C. Marais, "At least three scales of convection in a mantle with strongly temperature-dependent viscosity," Physics of the Earth and Planetary Interiors **188**, 132–141 (2011).

⁶X. Bao, *Hotspots from Top to Bottom*, Ph.D. thesis, University of California, Los Angeles (2024).

⁷A. Prasad and R. Adrian, "Stereoscopic particle image velocimetry applied to liquid flows," Experiments in fluids 15, 49–60 (1993).

⁸S. M. Soloff, R. J. Adrian, and Z.-C. Liu, "Distortion compensation for generalized stereoscopic particle image velocimetry," Measurement science and technology 8, 1441 (1997).

⁹C. Willert, "Stereoscopic digital particle image velocimetry for application in wind tunnel flows," Measurement science and technology **8**, 1465 (1997).

- ¹⁰K. H. Kang, S. J. Lee, C. M. Lee, and I. S. Kang, "Quantitative visual-974 ization of flow inside an evaporating droplet using the ray tracing method," 975 Measurement Science and Technology 15, 1104 (2004).
- Minor, P. Oshkai, and N. Djilali, "Optical distortion correction for liquid977 droplet visualization using the ray tracing method: further considerations," 978
 Measurement Science and Technology 18, L23 (2007).
- 12 K. Zha, S. Busch, C. Park, and P. C. Miles, "A novel method for correc-980 tion of temporally-and spatially-variant optical distortion in planar parti-981 cle image velocimetry," Measurement Science and Technology 27, 085201982 (2016).
 - ¹³Z. Gao, H. Radner, L. Büttner, H. Ye, X. Li, and J. Czarske, "Distortion984 correction for particle image velocimetry using multiple-input deep convo-985 lutional neural network and hartmann-shack sensing," Optics Express 29,986 18669–18687 (2021).
 - ¹⁴G. E. A. Meier, "Hintergrund-schlierenverfahren," (1999).

928

929

930

931

932

937

938

939

940

941

942

943

944

945 946

947

948

949

950

951

952 953

954

955

956

957

958

959

960

961

962

963

964

965

966

967

968

969

970 971

- ¹⁵M. Raffel, "Background-oriented schlieren (bos) techniques," Experiments₉₈₉ in Fluids **56**, 1–17 (2015).
- ¹⁶F. Nicolas, V. Todoroff, A. Plyer, G. Le Besnerais, D. Donjat, F. Micheli,⁹⁹¹
 F. Champagnat, P. Cornic, and Y. Le Sant, "A direct approach for instan-⁹⁹²
 taneous 3d density field reconstruction from background-oriented schlieren⁹⁹³
 (bos) measurements," Experiments in fluids 57, 1–21 (2016).
- ¹⁷S. Cai, S. Zhou, C. Xu, and Q. Gao, "Dense motion estimation of particle995 images via a convolutional neural network," Experiments in Fluids 60, 1–16996 (2019).
- ¹⁸M. Morimoto, K. Fukami, and K. Fukagata, "Experimental velocity data₉₉₈ estimation for imperfect particle images using machine learning," Physics₉₉₉ of Fluids 33 (2021).
- ¹⁹O. Ronneberger, P. Fischer, and T. Brox, "U-net: Convolutional net₁₀₀₁ works for biomedical image segmentation," in *Medical image computing*₀₀₂ and computer-assisted intervention–MICCAI 2015: 18th international con₁₀₀₃ ference, Munich, Germany, October 5-9, 2015, proceedings, part III 18₀₀₄ (Springer, 2015) pp. 234–241.
- ²⁰M. Born and E. Wolf, Principles of optics: electromagnetic theory of prop₁₀₀₆ agation, interference and diffraction of light (Elsevier, 2013).
- ²¹H. Richard and M. Raffel, "Principle and applications of the background₀₀₈ oriented schlieren (bos) method," Measurement science and technology 12₁₀₀₉ 1576 (2001).
- ²²P. K. Panigrahi and K. Muralidhar, Schlieren and shadowgraph methods in heat and mass transfer, Vol. 2 (Springer, 2012).
- ²³C. Lithgow-Bertelloni, M. Richards, C. Conrad, and R. Griffiths, "Plume₀₁₃ generation in natural thermal convection at high rayleigh and prandtl num₁₀₁₄ bers," Journal of Fluid Mechanics 434, 1–21 (2001).
- ²⁴C. Liu et al., Beyond pixels: exploring new representations and application ξ_{0.16} for motion analysis, Ph.D. thesis, Massachusetts Institute of Technology (2009).
- ⁹⁷² ²⁵F. Scarano and M. L. Riethmuller, "Advances in iterative multigrid piv im-⁹⁷³ age processing," Experiments in fluids **29**, S051–S060 (2000).

- ²⁶W. H. Newsome, Experimental investigation of mass transport, dynamics, and stirring in isolated thermal plumes, Ph.D. thesis, University of Michigan (2011).
- ²⁷J. Westerweel, "Efficient detection of spurious vectors in particle image velocimetry data," Experiments in fluids 16, 236–247 (1994).
- ²⁸ A. Davaille, A. Limare, F. Touitou, I. Kumagai, and J. Vatteville, "Anatomy of a laminar starting thermal plume at high prandtl number," Experiments in Fluids **50**, 285–300 (2011).
- ²⁹A. Buades, B. Coll, and J.-M. Morel, "Non-local means denoising," Image Processing On Line 1, 208–212 (2011).
- ³⁰J. Serra, *Image analysis and mathematical morphology* (Academic Press, Inc., 1983).
- ³¹L. K. Rajendran, S. P. Bane, and P. P. Vlachos, "Piv/bos synthetic image generation in variable density environments for error analysis and experiment design," Measurement Science and Technology 30, 085302 (2019).
- ³²D. A. Ham, P. H. J. Kelly, L. Mitchell, C. J. Cotter, R. C. Kirby, K. Sagiyama, N. Bouziani, S. Vorderwuelbecke, T. J. Gregory, J. Betteridge, D. R. Shapero, R. W. Nixon-Hill, C. J. Ward, P. E. Farrell, P. D. Brubeck, I. Marsden, T. H. Gibson, M. Homolya, T. Sun, A. T. T. McRae, F. Luporini, A. Gregory, M. Lange, S. W. Funke, F. Rathgeber, G.-T. Bercea, and G. R. Markall, *Firedrake User Manual*. Imperial College London and University of Oxford and Baylor University and University of Washington, first edition ed. (2023).
- ³³Z. Wang, "Image quality assessment: from error visibility to structural similarity," IEEE transactions on image processing **13**, 600–612 (2004).
- ³⁴J. Whitehead, A. Cotel, S. Hart, C. Lithgow-Bertelloni, and W. Newsome, "Numerical calculations of two-dimensional large prandtl number convection in a box," Journal of fluid mechanics **729**, 584–602 (2013).
- ³⁵H. Jeffreys, "Some cases of instability in fluid motion," Proceedings of the Royal Society of London. Series A, Containing Papers of a Mathematical and Physical Character 118, 195–208 (1928).
- ³⁶N. Cagney, W. H. Newsome, C. Lithgow-Bertelloni, A. Cotel, S. R. Hart, and J. A. Whitehead, "Temperature and velocity measurements of a rising thermal plume," Geochemistry, Geophysics, Geosystems 16, 579–599 (2015).
- ³⁷G. Haller, "Lagrangian coherent structures," Annual review of fluid mechanics 47, 137–162 (2015).
- ³⁸J. H. Gladstone and T. P. Dale, "Xiv. researches on the refraction, dispersion, and sensitiveness of liquids," Philosophical Transactions of the Royal Society of London, 317–343 (1863).
- ³⁹S. Matt, G. Nootz, S. Hellman, and W. Hou, "Effects of optical turbulence and density gradients on particle image velocimetry," Scientific Reports 10, 2130 (2020).